第 21 回
核燃焼プラズマ
統合コード研究会

21st Burning Plasma Simulation Initiative (BPSI) Meeting

日時：2023 年 12 月 21 日(木)－22 日(金)
場所：九州大学筑紫キャンパス応用力学研究所
2 階大会議室　および　オンライン

(Ver. 1, 2024 年 3 月 1 日発行)

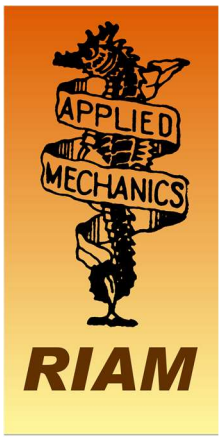

合同会合

第 21 回核燃焼プラズマ統合コード研究会

21st Burning Plasma Simulation Initiative (BPSI) Meeting

および

核融合エネルギーフォーラムサブクラスター会合
シミュレーションクラスター　炉心プラズマモデリングサブクラスター
プラズマ物理クラスター　定常運転・制御サブクラスター

(Ver.2)

日時：2023 年 12 月 21 日(木)－22 日(金)
場所：九州大学筑紫キャンパス　応用力学研究所 2 階大会議室　および　オンライン

12 月 21 日(木)

(特定研究「計測・シミュレーション・モデリングを組み合わせた統合診断」研究集会との合同会合)
（座長：糟谷）

9:45 – 10:00　講演 D-1　　糟谷（九大）
特定研究「計測・シミュレーション・モデリングを組み合わせた統合診断」の実施状況

10:00 – 10:30　講演 D-2　　古賀（兵庫県立大）
Research on a reconstruction method of micro-wave imaging using machine learning
機械学習を用いたマイクロ波イメージング再構成手法の研究

10:30 – 11:00　講演 D-3　　佐藤(雅)（核融合研）
Simulation data analysis of nonlinear structures of MHD instabilities in toroidal plasmas
トロイダルプラズマにおける MHD 不安定性の非線形構造のシミュレーションデータ解析

11:00 – 11:30　講演 D-4　　沼波（核融合研）
Development of a platform for quantitative understanding of plasma profile formation mechanisms using first-principal simulation, data science, and numerical measurement
プラズマ分布形成の定量的理解に向けた第一原理シミュレーションとデータ科学、数値計測による基盤開発

11:30 – 12:00　糟谷（九大）
discussion 議論（一部関係者のみ）

12:00 – 13:00　昼休み

13:00 – 13:20　会議登録 Registration
13:20 – 13:30　事務連絡 Business announcement

(座長：村上)
13:30 – 13:55　講演 1-1　　本多 (京大)
Assessment and feasibility study of core plasma performance for JA-DEMO using GOTRESS+
13:55 – 14:20　講演 1-2　　福山 (京大)
Progress of integrated code TASK and the development of interface with IMAS
14:20 – 14:40　講演 1-3　　持永 (九大)
Effect of toroidal rotation on impurity transport in tokamak improved confinement
14:40 – 14:55　講演 1-4　　田原 (京大)
The effect of beam-beam coulomb collisions on the energetic particle distribution in LHD

14:55 – 15:15　集合写真 group photo、休憩 break

(座長：福山)
15:15 – 15:40　講演 1-5　　矢木 (量研)
GPU acceleration of RMHD model and application to particle transport in plasma peripheral
15:40 – 16:05　講演 1-6　　奴賀 (核融合研) online
Degradation of fast-ion confinement depending on the neutral beam power without EP-driven instability in LHD
16:05 – 16:30　講演 1-7　　森下 (京大)
Development of an adaptive predictive control system using data assimilation at LHD
16:30 – 16:45　講演 1-8　　佐藤(真) (総研大)
Study of model based control for tokamak plasma profile
16:45 – 17:00　講演 1-9　　鈴木 (総研大)
Prediction of radiative collapse by analyzing videos of plasma discharge with CNN in LHD

17:00　散会

12 月 22 日(金)

9:00 – 10:30　ポスター講演 Poster
（online, 開室 start 8:50、閉室 end 12:50）

10:30 – 10:40　休憩

（座長：糟谷）
10:40 – 11:05　講演 2-1　　相羽（量研) online
Identification of plasma conditions affecting MHD stability in QH-mode and ELMy H-mode plasmas in DIII-D
11:05 – 11:30　講演 2-2　　佐々木（日大) online
Interaction between turbulence and zonal flows in the presence of mean shear flow
11:30 – 11:45　講演 2-3　　竹本（名古屋大) online
Comparison of W spatial distribution and time evolution by impurity transport calculation with soft X-ray measurement data

(Session Leader：村上)
11:45 – 12:05　議論 Discussion
12:05 – 12:10　事務連絡 Business announcement

12:10 – 13:30　昼休み Lunch break

(ワークショップ「不純物輸送」 Lunch time workshop “Impurity transport”
12:15 – 13:00 林（QST)、藤田（名大)、糟谷（九大) online
昨年に続く共同研究作業会を昼休みに開催します、関係者のみによる集まりです)

(核融合エネルギーフォーラムサブクラスターとの合同会合)
13:30 – 13:40　林（QST）
連絡事項
13:40 – 14:10　宮戸（QST）
IFERC 計算機シミュレーションセンターの現状報告
14:10 – 14:40　横山（核融合研）
ITER に於ける統合モデリング活動の報告
14:40 – 15:10　若月（QST）
ITPA 統合運転シナリオグループ活動報告
15:10 – 15:30　星野（慶應大）
炉心プラズマ＋炉工学炉材料モデリングサブクラスター合同会合の報告
15:30 – 16:00　林（QST）
今後の予定の議論

16:00　散会

Poster number

21th BPSI meeting (2023.12)
(Ver.1)

(コアタイム 前半: 奇数番、後半: 偶数番)

PA-1 村上定義 (京大) S. Murakami
Modeling of ECH supra-thermal electron transport in the presence of magnetic and electrostatic fluctuations

PA-2 成田絵美 (京大) E. Narita
Introduction of hydrogen isotope effects to a turbulent transport model DeKANIS and its application to integrated simulations

PA-3 登田慎一郎 (核融合研) S. Toda
Research of turbulent transport due to dissipative trapped electron mode in tokamak plasmas

PA-4 糟谷直宏 (九大) N. Kasuya
Development of integrated turbulence diagnostic simulator and its application to torus device measurement

PA-5 福永龍平 (京大) R. Fukunaga
Verification of charge separation model in generation of radial current with multi-fluid transport code TASK/TX

PA-6 古田原拓実 (日大) T. Kodahara
Extraction of abrupt turbulence driven particle transport using multi-field SVD

PA-7 可児和寿 (名大) K. Kani
Optimizations of NB deposition calculations in the integrated code

PA-8 桑宮幸佑 (九大) K. Kuwamiya
Simulation of PCI experimental diagnostic for density fluctuations in tokamak plasmas

PA-9 宮本琉耶 (九大) R. Miyamoto
Evaluation of nonlinear mechanism to induce inward turbulent particle fluxes in tokamaks

PA-10 小山一輝 (九大) K. Oyama
Analysis of parallel flow shear driven mode including effect of finite ion temperature gradient

「計測・シミュレーション・モデリングを組み合わせた統合診断」

特定研究の実施状況

Present status of designated joint research “Synthetic diagnostics combining measurement, simulation and modeling”

N. Kasuya
RIAM, Kyushu Univ.

九州大学応用力学研究所では「計測・シミュレーション・モデリングを組み合わせた統合診断」をテーマとした特定共同研究を実施している。本特定研究では、様々な分野で行われている実験計測、複合シミュレーション、データ駆動モデリングを組み合わせた統合的診断手法の共通性や応用性を探ることで、液体・気体・プラズマのミクロ・マクロ的様相を理解するためのさらなる手法の進展を目指している。
以下の 6 件のサブテーマを実施している。

・データ駆動科学的手法を用いた非平衡開放系の時空間ダイナミクス研究 (研究代表者 日本大学 佐々木真准教授)
・計測との比較に向けた不純物輸送の統合モデリング (研究代表者 京都大学 本多充教授)
・機械学習を用いたマイクロ波イメージング再構成手法の研究 (研究代表者 兵庫県立大学 古賀麻由子准教授)
・トロイダルプラズマにおける MHD 不安定性の非線形構造のシミュレーションデータ解析 (研究代表者 核融合科学研究所 佐藤雅彦助教)
・直線磁化プラズマにおける乱流構造の解析 (研究代表者 九州大学 山田琢磨教授)
・プラズマ分布形成の定量的理解に向けた第一原理シミュレーションとデータ科学、数値計測による基盤開発 (研究代表者 核融合科学研究所 沼波政倫教授)

本セッションではそのうちより 3 件の研究進捗状況を発表いただき、相互理解を深めるとともに、共同研究進展の可能性について議論する。

Research on a reconstruction method of micro-wave imaging using machine learning

Mayuko Koga

Graduate School of Engineering, University of Hyogo, Himeji, Hyogo 671-2280, Japan

Plasma imaging plays a pivotal role in fusion plasma study. Sub-microwave and microwave diagnostic techniques, such as reflectometry, offer the advantage of straightforward-identification of measured points [1]. To overcome the challenge of achieving high resolution imaging with a limited number of antennas, there is a need to explore method for image reconstruction from sparse measurements. Tsuchiya *et al.* previously demonstrated the feasibility of reconstructing simple images from complex-amplitude microwave data using Tikhonov-Phillips regularization techniques [2]. However, generating videos from numerous images remains impractical due to the extensive computational time required for each image reconstruction. In this paper, perform the principal verification of reconstructing object surface images by using deep learning.

In various fields, the significance of the quality and scale of training data is well-recognized for supervised learning. Ideally, training data should be sourced from actual plasma experiments. However, due to the inherent difficulty of controlling the cutoff surface pattern in plasma experiments, we undertook numerical calculations of reflected microwave distribution across a wide range of patterns. Subsequently, this dataset, consisting of pattern-distribution pairs, was employed for our training purposes. We made objects with a protrusion. The footprint of the protrusion is set to elliptical, whose length of major and minor axis are randomly set in the range of 1 mm to 65 mm, respectively. The protrusion shape is a Gaussian function like, whose top is 1 mm height. The position and the rotation angle of the protrusion are also randomly set. The reflectance of the object is set to 1. Thirty gigahertz microwave is irradiated to the object and completely reflected at the surface of the object. The reflected microwave signals are received by an antenna array. The antenna array consists of horn antennas arranged in 16 × 16 pieces, with each antenna having a size of 10 mm square. We randomly changed the structure of protrusion and calculated the corresponding received microwave signals.

We used convolutional neural network (CNN) as the neural network for deep learning. We tried three patterns as input channels, absolute values of complex amplitudes, absolute values of complex amplitudes and phase, real and imaginary part of complex amplitudes. The image of received microwave signals is input into the network with 16 × 16 pixels. It passes through a convolutional layer (karnel size: 6 × 6, number of filters: 50) and a max pooling layer (window

size: 2 × 2). After that, it passes through 3 layers of the fully connected layer which contains 50 perceptron and one reshape layer. Tanh function was used as the activation function. After passing through the reshape layer, a predictive image of object surface is outputted with 128 × 128 pixels. This means that the output image is upconverted from the input image.

Figure 2 and 3 show the example of reconstruction. The input channels take absolute values of complex amplitudes (Fig. 2) and real part and imaginary part of complex amplitudes (Fig. 3). The color bars mean normalized intensities in (a), surface positions in the depth direction in (b) and (c). The numbers above images show the numbers of training data used for each model. Both figures show that reconstructed images capture features of object images. As the number of training data increases, it is clear that small structures of objects are well reproduced. It was found that two types of input data (real-imaginary part) are better than one type of input data (absolute values). Reconstruction calculations on a trained model takes about milliseconds computing time, and could be applied for real-time feedback, etc in future.

References

[1] Y. Nagayama, N. Ito, D. Kuwahara, H. Tsuchiya, and S. Yamaguchi, Rev. Sci. Instrum. **88**, 044703 (2017).

[2] H. Tsuchiya, N. Iwama, S. Yamaguchi, R. Takenaka and M. Koga, Plasma Fusion Res. **14**, 3402146 (2019).

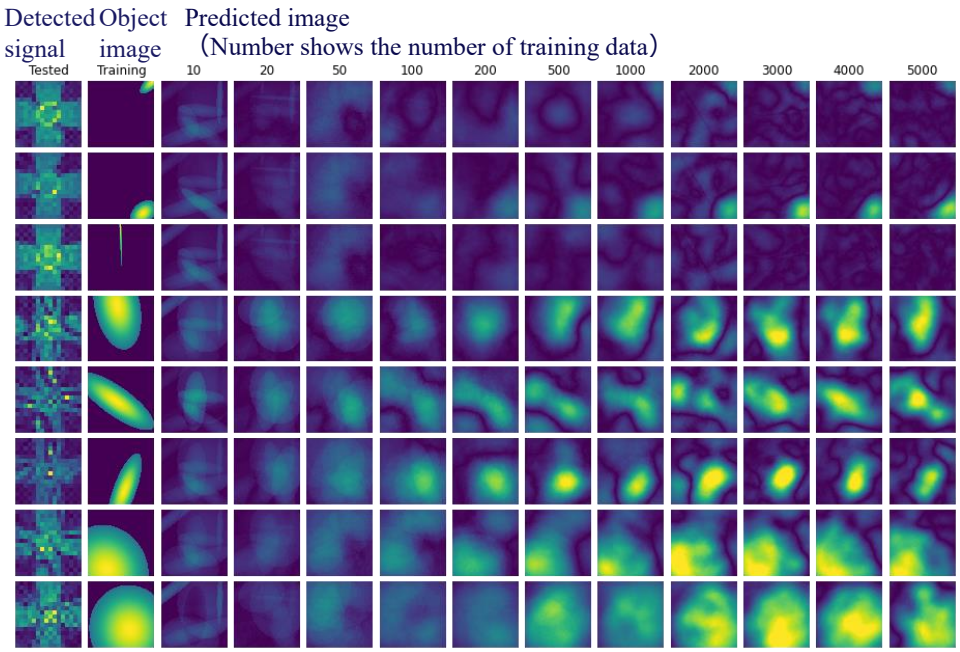

Fig. 1. (a) Received microwave signals, (b) object surface images and (c) corresponding reconstructed surface images by models with different numbers of training data. The input channels take absolute values of complex amplitudes. The numbers above images show the numbers of training data.

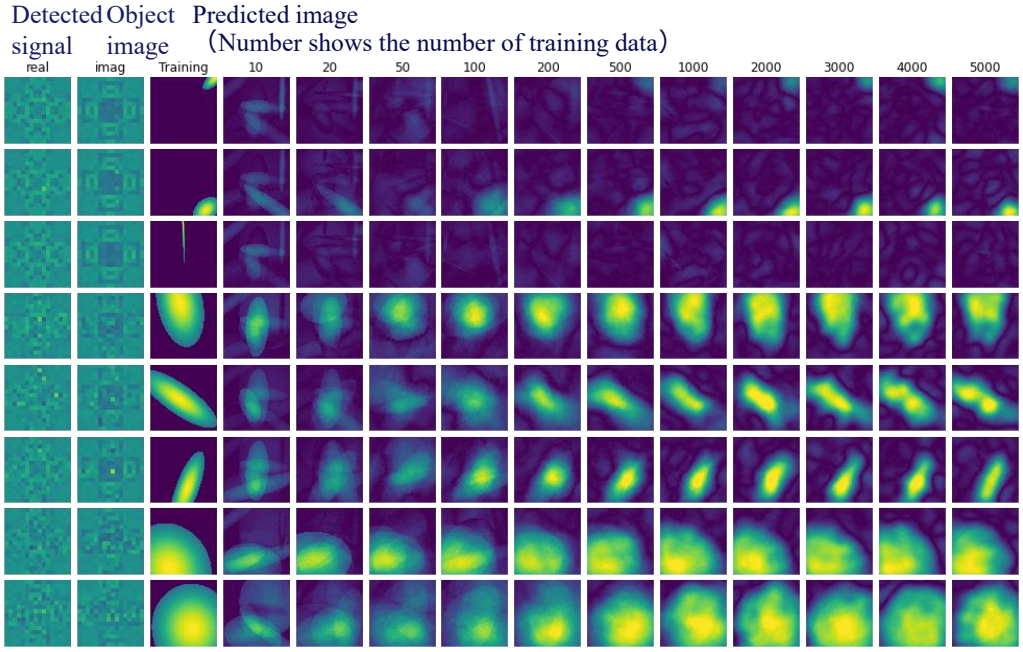

Fig. 2. (a) Received microwave signals, (b) object surface images and (c) corresponding reconstructed surface images by models with different numbers of training data. The input channels take real part and imaginary part of complex amplitudes. The numbers above images show the numbers of training data.

Simulation data analysis of nonlinear structures of MHD instabilities in toroidal plasmas (Analysis of infernal modes in tokamak plasmas)

M. Sato[1], Y. Todo[1], N. Aiba[2] and M. Takechi[2]
[1]National Institute for Fusion Science, Toki, Gifu, 509-5929, Japan
[2]National Institutes for Quantum Science and Technology, Naka, Ibaraki, 311-0193, Japan

In order to realize a steady-state fusion reactor, high beta plasma must be stably confined for a long time. In high beta plasmas, the bootstrap current, which is a non-inductive current, increases and discharges with an increased proportion of bootstrap current are one of the steady-state operation scenarios in tokamak plasmas. Since the bootstrap current takes its maximum value away from the magnetic axis, resulting in a flat q-profile or negative magnetic shear configuration, the magnetic shear in the core region becomes weak. It has been pointed out that the presence of a large pressure gradient in such a weak magnetic shear region can lead to infernal modes with low toroidal mode number[1]. In [2, 3], the linear ideal MHD analyses showed that the occurrence of poloidal beta collapse in JT-60U is consistent with the violation of the stability boundary of the ideal infernal modes. However, since the previous studies are based on the linearized ideal MHD model, the influence of the saturated state of both the ideal infernal modes and the resistive infernal modes on the plasma confinement has not been clarified yet. For the highly accurate evaluation of the beta limit, not only linear stability but also nonlinear saturated state should be investigated for both the ideal and the resistive modes. For the evaluation of the beta limit, the effects of kinetic thermal ions might be important since the linear growth rate of the instabilities becomes small for the plasmas near the beta limit. For example, in the LHD plasmas, it was found that the effects of the kinetic thermal ions play an important role for the stability beta limit[4]. In this study, kinetic-MHD hybrid simulation analysis for the infernal modes is carried out in order to clarify the effects of the kinetic thermal ions on the linear stability and the saturated states of the infernal modes.

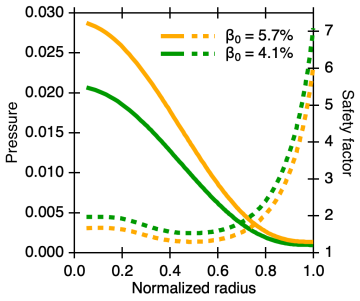

Fig.1 Profiles of pressure (solid curve) and the safety factor (dashed curve) for the MHD equilibria analyzed in this study.

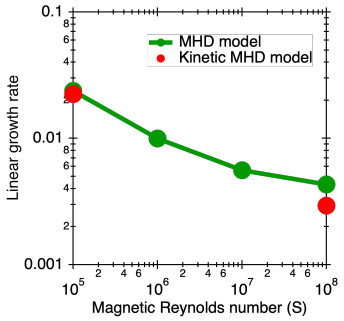

Fig.2 Dependence of the linear growth of the n=3 mode on the magnetic Reynolds number (S) for β_0 = 5.7%.

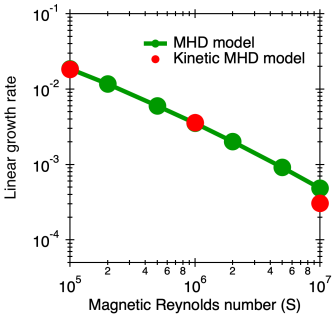

Fig.3 Dependence of the linear growth of the n=3 mode on the magnetic Reynolds number (S) for β_0 = 4.1%.

The numerical calculations are performed by MIPS code (MHD model) and MEGA code (Kinetic-MHD hybrid model) In the MEGA code, thermal ions are treated by the drift kinetic model and the electrons are treated by the fluid model[4, 5]. The periodic boundary condition is imposed at $\phi = 0$ and $\phi = 2\pi/3$ so that only the n = 3 mode and its harmonics are included where ϕ is the toroidal angle. In this study, two MHD equilibria with circular poloidal cross section are analyzed. Figure 1 shows the profiles of the pressure and the safety factor of the two equilibria. The central beta value β_0 of the two equilibria is β_0 = 5.7% and β_0 = 4.1%. For β_0 =5.7%, an n=3 ideal infernal mode is unstable where n is the toroidal mode number. On the other hand, for β_0 = 4.1%, the n=3 ideal infernal mode is stable while the n=3 resistive infernal mode is unstable.

Figure 2 shows the dependence of the linear growth rate on the magnetic Reynolds number (S) for β_0 = 5.7%. Although the

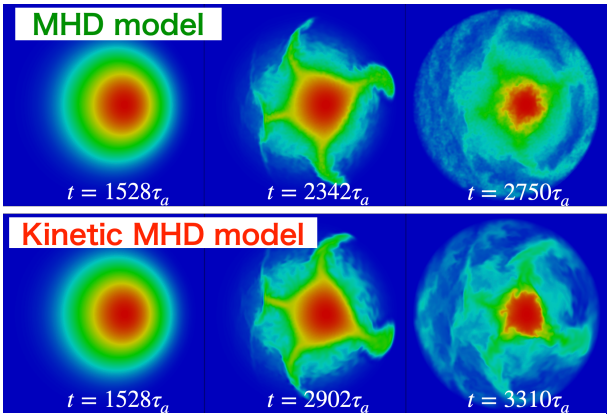

Fig.4 Time evolution of the pressure profile on a poloidal cross section obtained from the MHD model (the upper rows) and the kinetic-MHD hybrid model (the lower rows) for (β_0, S) = (5.7%, 10^8).

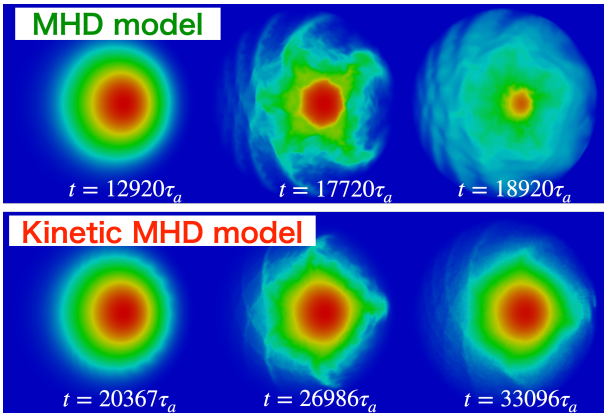

Fig.5 Time evolution of the pressure profile on a poloidal cross section obtained from the MHD model (the upper rows) and the kinetic-MHD hybrid model (the lower rows) for (β_0, S) = (4.1%, 10^7).

linear growth rate depends on the S number in low S regime, the linear growth rate becomes independent on the S number in high S regime, which indicates that the unstable mode is an ideal mode. The kinetic-MHD hybrid simulations with kinetic thermal ions were conducted for $S=10^5$ and $S=10^8$, with their linear growth rates illustrated by the red circles. For $S=10^5$, the linear growth rate obtained from the kinetic-MHD hybrid model with kinetic thermal ions is almost the same as that obtained from the MHD model without kinetic thermal ions. When $S=10^8$, the linear growth rate obtained from the kinetic-MHD hybrid model with kinetic thermal ions is smaller than that obtained from the MHD model without kinetic thermal ions. The linear growth rates for $\beta_0 = 4.1\%$ obtained from the MIPS code and the MEGA code are shown in Fig. 3. The linear growth rate obtained from the MHD model without kinetic thermal ions decreases as the S number increases, indicating a resistive infernal mode remains unstable. For $S=10^7$, the linear growth rate obtained from the kinetic-MHD hybrid model with kinetic thermal ions is smaller than that for the MHD model without kinetic thermal ions.

Figure 4 shows the time evolution of the pressure profile on a poloidal cross section for (β_0, S) = (5.7%, 10^8). For both the models, at the saturated state, the influence of the instabilities expands to the almost the whole region and the pressure profile is significantly flattened. Thus, the influence of the effects of the kinetic thermal ions is weak for the ideal infernal modes. Figure 5 shows the time evolution of pressure profile on a poloidal cross section for (β_0, S) = (4.1%, 10^7). The pressure profile obtained from the MHD model is significantly flattened at the saturated state. On the other hand, for the kinetic-MHD hybrid model, the pressure profile is not flattened at the saturated state. This indicates that kinetic thermal ions play an essential role for the suppression of pressure profile flattening due to slowly growing resistive MHD instabilities.

[1] J. Manickam et al, Nucl. Fusion **27** (1987) 1461.
[2] T. Ozeki et al., Nucl. Fusion **33** (1993) 1025.
[3] T. Ozeki et al., Nucl. Fusion **35** (1995) 861.
[4] M. Sato and Y. Todo, Nucl. Fusion **61** (2021) 116012.
[5] Y. Todo et al., Plasma Phys. Control. Fusion **63** (2021) 075018.

Assessment and feasibility study of core plasma performance for JA-DEMO using GOTRESS+

M. Honda, N. Aiba[1], M. Furukawa[2], Y. Masamoto[2], and R. Otani

Kyoto University, Nishikyo-ku, Kyoto 615-8530 Japan

[1]National Institutes for Quantum Science and Technology, Rokkasho, Aomori 039-3212 Japan

[2]Tottori University, Tottori, Tottori 680-8550 Japan

GOTRESS+ extension for burning plasmas

In DEMO, a plasma is alpha-heated almost exclusively in a stationary state. Given that auxiliary heating systems have functioned as actuators to control the plasma, in burning plasmas, where the contribution of auxiliary heating to the total heating power is quite small, it is not always obvious whether and how a stationary state can be achieved and then be stably maintained. Therefore, it is important to verify them through numerical simulations. Recent updates to convergence algorithms in GOTRESS enable the robust identification of stationary states while accounting for alpha heating and large radiation loss channels, both of which are unique to burning plasmas. GOTRESS+, a novel integrated model GOTRESS+ [1] as illustrated in Fig. 1, is therefore ready to perform predictive burning plasma simulations. We verify whether the target values for the JA-DEMO plasma [2] can be achieved with GOTRESS+. The plasma confinement performance is greatly affected by the choice of turbulent transport model. In this case, the CDBM turbulent transport model [3] was selected.

Assessment of JA-DEMO operation scenario with ECH only

Electron cyclotron heating (ECH) can realize a localized absorption profile, allowing adjustments to the current profile shape to reduce magnetic shear locally and promote internal transport barrier (ITB) formation. The research investigates whether it is possible to achieve the target values with less power by adjusting the injection parameters of ECRF waves. For simplicity, it assumes that the ECH power is injected from a single launcher.

Figure 2 shows the summary of the GOTRESS+ simulation results for the scenario with ECH only. In this case, O-mode wave with 185GHz and 90MW was injected from the mirror with toroidal angle of 150° and poloidal angle of 25° located at (R,Z)=(11.5,0.9) in meters, as shown in Fig. 2 (a). As evident from Fig. 2 (d), the localized absorption of the EC wave results in 2.9 MA EC current generation. Consequently, as observed in Fig. 2 (b) near the absorption peak, a negative magnetic shear is formed, suppressing turbulent transport there and leading to the formation of the electron and ion ITBs, as shown in Figs. 2 (f) and (g). In this case, all of the figures of merit meet the target values [2]. However, we note that the global ideal MHD stability has not been achieved, even if ion diamagnetic drift stabilization is taken into account. To achieve the target value of Q=13, it is necessary to obtain a fusion output of at least 1.17GW with ECH power of 90MW, which inevitably requires high plasma confinement through ITB formation. This, in turn, necessitates a high β value, making MHD modes more prone to be unstable. Among the target values, the requirement for the Q value seems the most stringent, and relaxing this target value somewhat could allow for an MHD-stable scenario.

References

[1] M. Honda et al., Nucl. Fusion **61**, 116029 (2021).

[2] Y. Sakamoto et al., IAEA 27th Fusion Energy Conf., FIP/3-2, Gandhinagar (2018).

[3] M. Honda and A. Fukuyama, Nucl. Fusion **46**, 580 (2006).

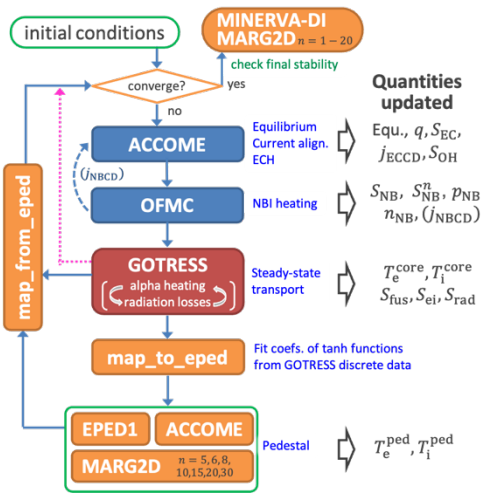

Fig. 1: The flowchart of a GOTRESS+ simulation. When not using EPED1, one proceeds the convergence

check along the magenta dashed arrow extending from GOTRESS after finishing a GOTRESS simulation. If the NB-driven current calculated by OFMC is used in the next ACCOME calculation as an option, the driven current data is passed along the blue dashed arrow.

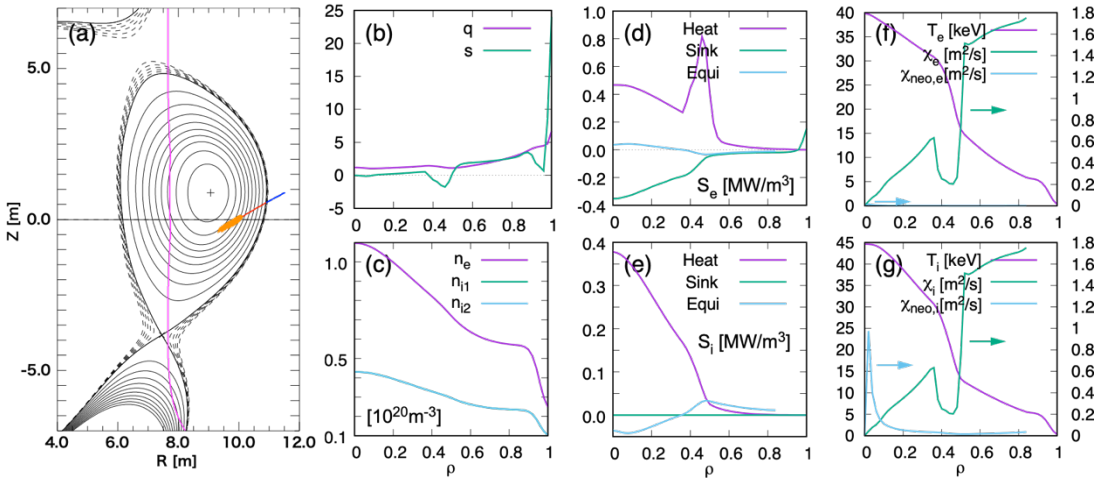

Fig. 2: GOTRESS+ prediction of stationary-state profiles for the JA-DEMO scenario with ECH only. (a) The equilibrium with EC ray and the resonant layer superimposed, (b) the safety factor q and the magnetic shear s profiles, and (c) density profiles are given, while profiles of (d) the heat source, the sink, (f) the temperature T and diffusivity c for electrons and (e)(g) those for ions are calculated

GPU acceleration of RMHD model and application to particle transport in plasma peripheral

M. Yagi, H. Todoroki, N. Kasuya

National Institutes for Quantum and Radiological Science and Technology,
Rokkasho Fusion Institute, Rokkasho, Aomori, Japan
Research Institute for Applied Mechanics, Kyushu University, Kasuga, Fukuoka, Japan

1. Introduction

In fusion plasmas, the burn control is important issue to sustain the self-ignition condition. To understand particle transport mechanism is essential to supply the fuel ions at plasma peripheral. We are developing the transport-MHD model based on the reduced MHD (RMHD) model to investigate this problem. In the present work, the implementation of R5F code (5-field RMHD) on GPU is performed using OpenACC. It is found that the subroutine where nonlinear coupling is calculated using the pseudo-spectral method is the most expensive part of the code. We have reduced communications between CPU and GPU in between cuFFT calls. As the result, the elapse time of this subroutine is reduced more than half.

2. Numerical Scheme and Parallel Algorithms

The code is described on the cylindrical coordinates (r, θ, ζ), where the finite difference method is applied for r direction and the spectral method is applied for θ and ζ directions. For parallel algorithms, we have adopted the 1-dimensional domain decomposition method. The 5-field RMHD model is schematically written as

$$\frac{\partial}{\partial t} U = L(U) + N(U, U)$$

where U is the vector and L, N are the linear and nonlinear operators, respectively. The linear terms are solved by Crank Nicolson implicit method and the nonlinear terms are evaluated by the predictor-corrector method (namely, the first step is the explicit and the second step is the implicit way). They are given by

$$\frac{U^{n+1/2} - U^n}{\Delta t/2} = L\left(\frac{U^{n+1/2} + U^n}{2}\right) + N(U^n, U^n)$$

$$\frac{U^{n+1} - U^n}{\Delta t} = L\left(\frac{U^{n+1} + U^n}{2}\right) + N\left(U^{n+1/2}, U^{n+1/2}\right)$$

The matrix inversion can be performed by the LAPACK library.

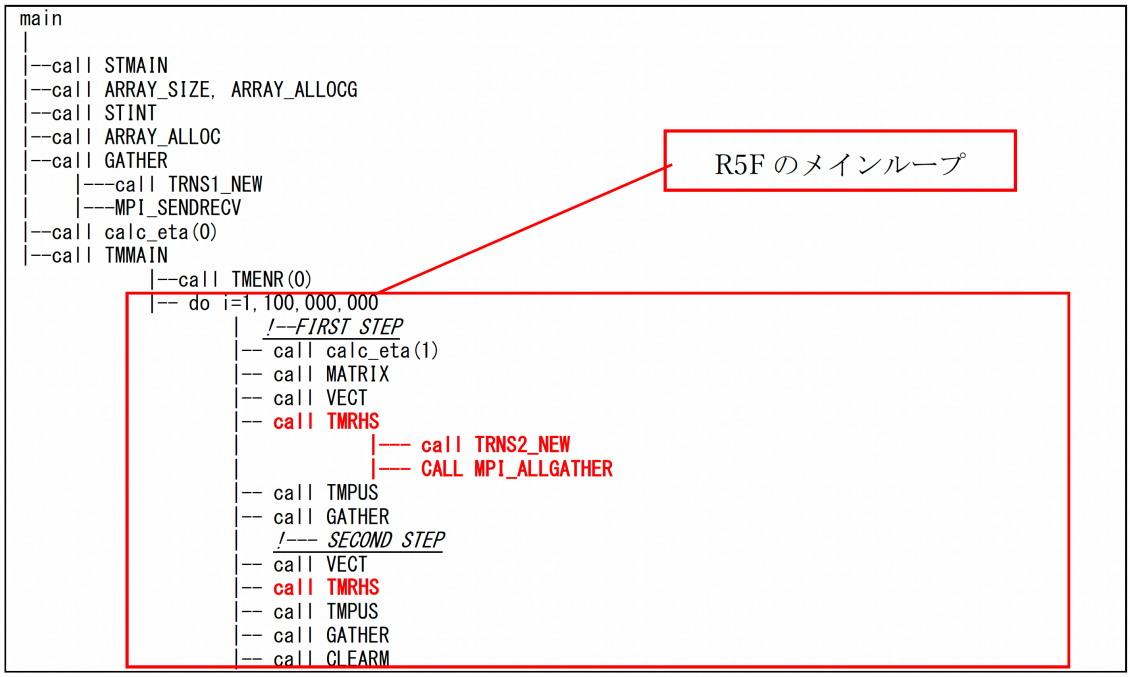

Figure 1: Main loop in R5F

The benchmark environment provides that Intel Xeon Gold 6248R (2.8GHz, 24cores) x2 for CPU and NVIDIA V100 GPUs with Nvlink 2.0 and 32GBx4 memory. For the compiler, NVIDIA HPC SDK 22.5 (nvfortran) and CUDA 11.4 is adopted. The compiler options are given by -O4 -fast -mcmodel=medium -fastsse -I/fftwpath/include -Mpreprocess -DUSEMPI2 for CPU execution and -O4 -fast -mcmodel=medium -fastsse -acc -Mcuda -I/cudadir/11.4/include -Mpreprocess -DCUFFT -DUSEMPI2

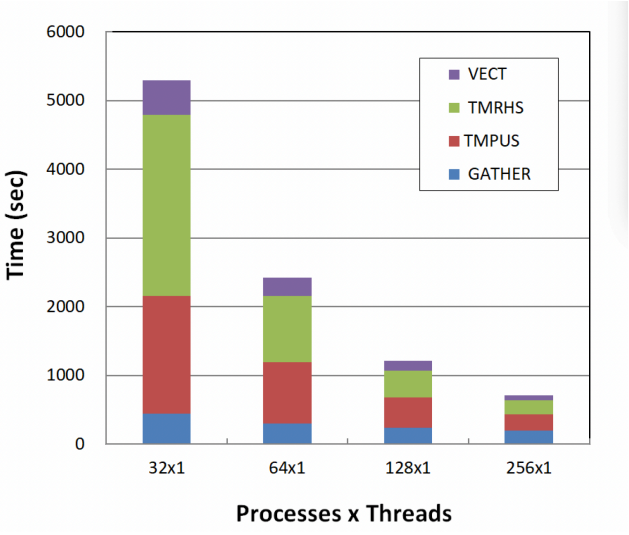

Figure 2: Cost evaluation for each subroutine using CPU version

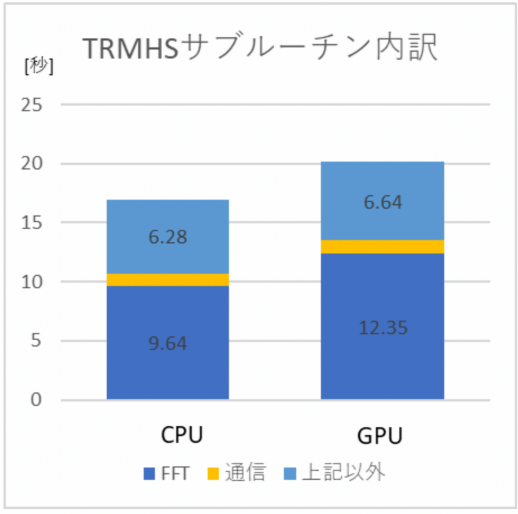

Figure 3: Comparison of execution time for TMRHS between CPU and GPU version

Figure 1 shows the main loop in R5F and we found that the cost of subroutine TMRHS is most expensive part shown in figure 2. As the first step, we simply replaced FFTW to cuFFT which is executed on GPU. It becomes slower than FFTW on CPU shown in figure 3. It is found that the elapse time for data transfer between CPU and GPU is dominant in FFT area for GPU version. If we compare the elapse time of FFT execution, cuFFT is roughly 44 times faster than FFTW. Therefore, the next step is to suppress frequent data copy between CPU and GPU. It can be done using enter data and exit data directive as well as kernels directive.

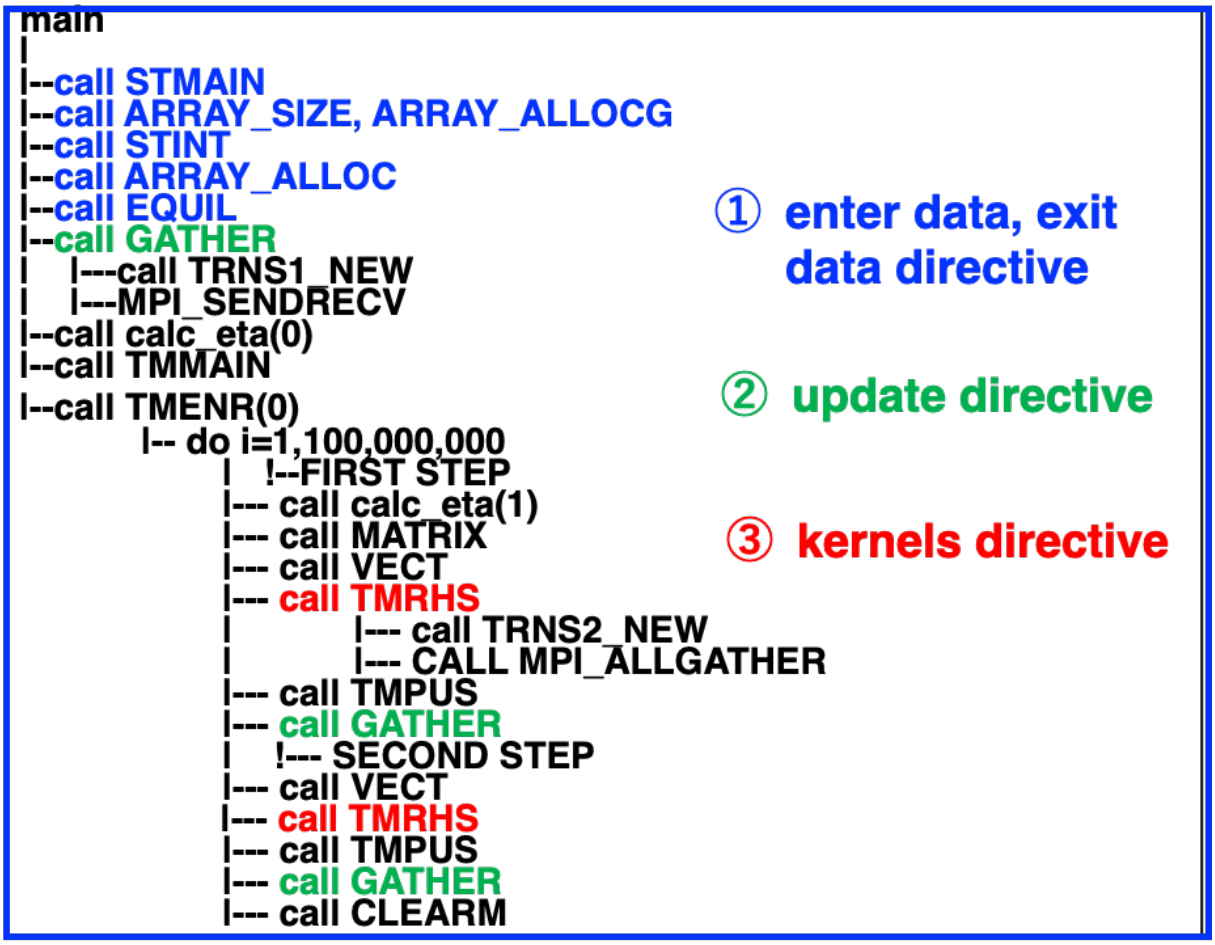

Figure 4: Enter data area is shown blue box.

The variables which are used by cuFFT can be stationed on GPU memory if we use enter data directive such as

```
!$acc enter data create(W1C(1:LYMED,1:KZMWD,S:E),…)
!$acc host data use device(W1C(1:LYMWD,1:KZWD,S:E),…)
DO I=S:E
istat=cufftExecZ2D(cuplan,W1C(1,1,I),W1R(1,1,I))
END DO
```

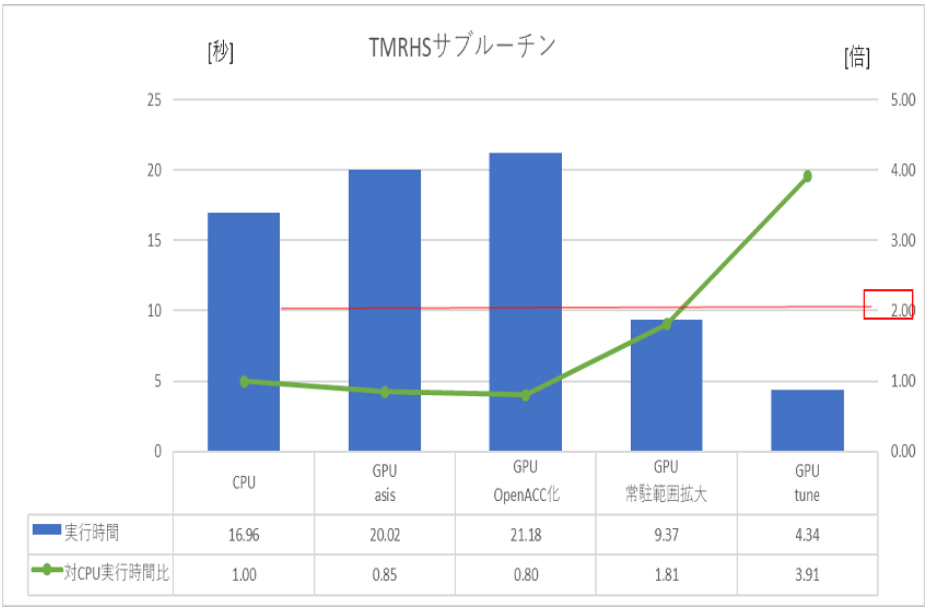

Figure 5: Tuning results the 4th bar (from left) shows the tuned result for 1GPU and the 5th bar the one for 4 GPUs.

The tuning results show that 1 GPU case is 1.81 times faster than CPU case and 4 GPU case is 3.91 times faster than CPU case. The key for GPU implementation is to suppress the communication between CPU and GPUs as much as possible. The off-load technique is essential for this purpose.

4. Summary and discussion

We have implemented 5-field RMHD model on GPU machine (SGI HPE8600). The goal is set that the elapse time of the subroutine TMRHS by GPU is more than double shorter over CPU version. The communications between CPU and GPU before and after the function call of cuFFT library are reduced using enter data directive. As the result, we obtained fairly good result. Also, we extended the 4 GPU use in a node. In this case, GPU version gives almost 4 times faster than that of CPU version. The optimization of MPI communication using NVLink for TMRHS should be performed. In addition, the subroutine GATHER should be implemented on GPU. There are left for future work.

Acknowledgements

The computations were carried out on SGI HPE8600 supercomputer at QST and JAEA. This work was supported in part by the Collaborative Research Program of Research Institute for Applied Mechanics, Kyushu University (2023CR-FP-25).

Degradation of fast-ion confinement depending on the neutral beam power without EP-driven instability in LHD

H. NUGA[1], R. SEKI[1,2], K. OGAWA[1,2], H. YAMAGUCHI[1,2], S. KAMIO[1], Y. FUJIWARA[1], Y. KAWAMOTO[1], M. YOSHINUMA[1], T. KOBAYASHI[1,2], Y. TAKEMURA[1], M. OSAKABE[1,2], M. ISOBE[1,2], M. YOKOYAMA[1,2]

[1]National Institute for Fusion Science, Toki, Japan
[2]The Graduate University for Advanced Studies, SOKENDAI, Toki, Japan

Introduction The physics of the fast-ion transport is the one of the important issue for the achievement of the magnetically confined fusion reactor. This is because the plasma temperature is sustained by the kinetic energy transfer from fast-ions generated by external heatings and fusion born alpha particles. For this reason, the fast-ion transport mechanism has been investigated in several magnetic confinement devices and simulations.

It is known that fast-ion confinement degrades with fast-ion-driven instabilities. The typical feature of this kind of loss is that the transport coefficient depends on the fast-ion pressure, unlike other fast-ion loss mechanisms. This feature is explained that the amplitude of the instability depends on the fast-ion pressure.

However, we observed the fast-ion confinement degradation depending on NB power even in MHD quiescent plasmas in the Large Helical Device (LHD). In this paper, we estimate the confinement degradation quantitatively through the neutron measurement and the integrated simulation.

Experimental apparatus In this paper, two external heating systems, ECH and NBIs are used. Plasmas are sustained by 3.8 MW ECH during each discharge. The magnetic configuration used in this experiment are (B_t, R_{ax}) = (2.75 T,3.6m), where B_t and R_{ax} are the toroidal magnetic field strength on the magnetic axis and the position of the magnetic axis with respect to the major radius, respectively. The direction of the magnetic field is couter clockwise.

The LHD is equipped with five neutral beams as shown in Figure 1. In this work, we focus on the tangential NB fast-ion. A positive ion-based perpendicular beam (NB#4) is used as a beam probe for the charge exchange spectroscopy (CXS) measurements.

Experimentl Scenario Figure 2 shows the typical waveform used in these experiments. The plasma discharges start at t = 3.3 s with 3.8 MW ECH. The first beam, NB#1, is injected from t = 3.3 s to t = 5.3 s. The second beam, NB#3 (or NB#2), is injected at t = 4.3 s. In this paper, the period from t = 3.3 s to t = 4.3 s is called the "single beam phase" and the period from t = 4.3 s to t = 5.3 s is called the "double beam phase". In addition, the case with NB#1 and NB#3 is called the "co-injection case" and the case with NB#1 and NB#2 is called the "balance injection case". NB#4 is injected repeatedly with a 20 ms pulse in each 200 ms from t = 3.32 s.

Experimental Results Figures 3 and 4 show the degradation of the fast-ion confinement due to the increase in NB power. To consider the difference in the beam injection energy, the y-axis value

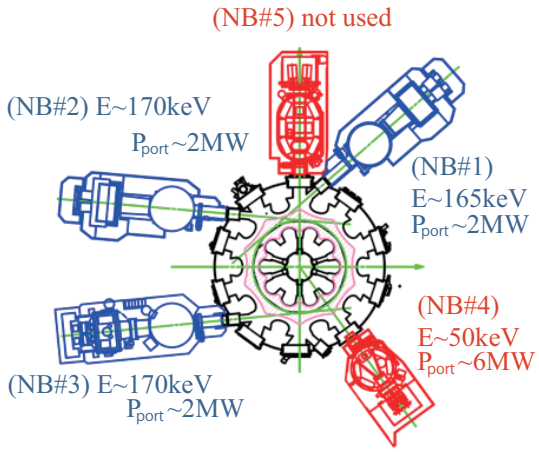

Figure 1: Top view of NBI system in the LHD. Typical beam injection energy and port-through power values are shown.

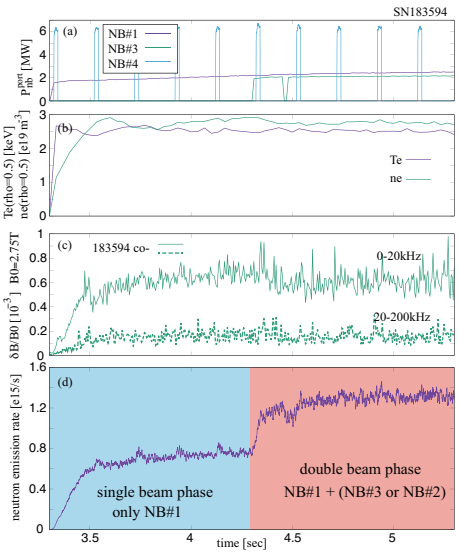

Figure 2: Typical waveform used in these experiments (shot number (SN) 183594). (a) the NB port-through power, (b) the electron temperature and density, (c) the magnetic fluctuation, and (d) the neutron emission rate.

is Sn divided by the sum of the tangential NB port-through power multiplied by the beam-thermal fusion cross-section and is normalized to that at t = 4.2 s.

Figure 3 shows that the neutron emission rate per beam power decreases by up to 20% after NB superpose. On the other hand, the amplitude of the magnetic fluctuation does not change after NB superpose as shown in Figure 2-(c). In addition, there are no significant variation in the electron temperature and density and NB shine-through rate after NB superpose. For these reasons, the fast-ion confinement degradation causes the decrease of the neutron emission rate per NB power. A similar reduction of the neutron emission rate per NB power appears in the balance injection case in the high-density discharges as shown in Figure 4. The neutron emission rate per NB power in the double beam phase exceeds that in the single beam phase for the low-density discharges because

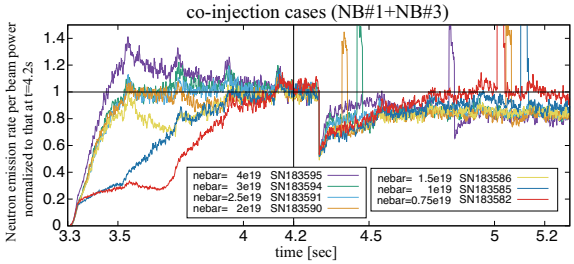

Figure 3: Time evolution of the neutron emission rate per beam power for the co- injection cases.

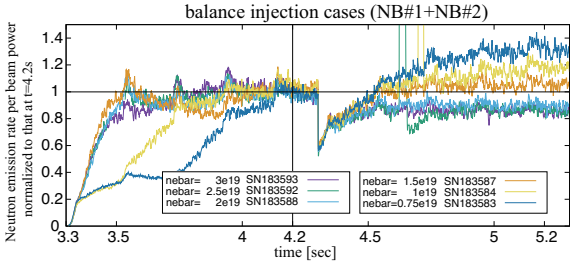

Figure 4: Time evolution of the neutron emission rate per beam power for the balance injection cases.

the beam-beam fusion reaction is not negligible. From these result, we can guess that the fast-ion confinement degradation also occurs in the balance injection cases and that the degradation may not be visible due to the beam-beam fusion reaction in the low-density discharges.

Analysis model To quantitatively estimate the degradation depending on NB power, we formulate the following model. The time derivative of the neutron emission rate, S_n, can be described as

$$\frac{\partial S_n}{\partial t} = S - \frac{S_n}{\tau_n^{\mathrm{cl}}} - \frac{S_n}{\tau_{\mathrm{cx}}^{\mathrm{amb}}} - \frac{P_{\mathrm{NB}} S_n}{\tau_{\mathrm{ano}}}, \tag{1}$$

where S is the sourve term of the neutron emission rate due to the beam injection, P_{NB} is the dimensionless factor indicating the sum of the tangential NB port-through power normalized to 1 MW, $\tau_n^{\mathrm{cl}}$is the neutron decay time due to the classical slowing down, $\tau_{\mathrm{cx}}^{\mathrm{amb}}$ is the time constant of the charge exchange loss, and τ_{no} is the time constant of the anomalous confinement degradation per 1 MW. The fourth term is the anomalous fast-ion loss, which is the focus of this paper. The source term S can be roughly expressed as follows,

$$S \sim C n_D^{\mathrm{bulk}} P_{\mathrm{NB}}, \tag{2}$$

where n_D^{bulk} is the bulk-deuteron density and C is a constant factor related to the fusion cross-section and the beam ion birth rate. The factor C can be viewed as a constant in a single discharge because the beam injection energy, shine-through rate, plasma density, and temperature are constant in both phases. By using values both in the single and double beam phases, we can obtain the following expression about the time constant of the anomalous degradation.

$$\tau_{\mathrm{ano}} = \frac{(\frac{\beta}{n_{D,d}} P_{\mathrm{NB,d}} - \frac{\alpha}{n_{D,s}} P_{\mathrm{NB,s}}) \tau_{\mathrm{cx}}^{\mathrm{amb}} \tau_{n,s}^{\mathrm{cl}} \tau_{n,d}^{\mathrm{cl}}}{\frac{\alpha}{n_{D,s}} \tau_{n,s}^{\mathrm{cl}} \tau_{n,d}^{\mathrm{cl}} + \frac{\alpha}{n_{D,s}} \tau_{\mathrm{cx}}^{\mathrm{amb}} \tau_{n,d}^{\mathrm{cl}} - \frac{\beta}{n_{D,d}} \tau_{n,s}^{\mathrm{cl}} \tau_{n,d}^{\mathrm{cl}} - \frac{\beta}{n_{D,d}} \tau_{\mathrm{cx}}^{\mathrm{amb}} \tau_{n,s}^{\mathrm{cl}}}, \tag{3}$$

where where subscripts "s" and "d" indicate the values in the single- and double-beam phases, $\alpha \equiv P_{\mathrm{NB,d}}/P_{\mathrm{NB,s}}$, and $\beta \equiv S_{n,d}/S_{n,s}$, respectively. The effective confinement time is given by

$$\left(\tau_{c,s}^{\mathrm{eff}}\right)^{-1} = \left(\tau_{\mathrm{cx}}^{\mathrm{amb}}\right)^{-1} + \left(\frac{\tau_{\mathrm{ano}}}{P_{\mathrm{NB,s}}}\right)^{-1}. \tag{4}$$

Simulation result with obtained τ_c^{eff} Figures 5 shows the time evolutions of the measured and simulated neutron emission rate for the co-injection case. Simulations with obtaind τ_c^{eff} have a good agreement in the range of 0.75×10^{19} m$^{-3} < \bar{n_e} < 3 \times 10^{19}$ m^{-3}. For this result, the obtained τ_c^{eff} is valid.

In contrast, eq. (3) can not be applied for the balance injection case because the beam-beam fusion is not ignorable. To apply the anomalous degradation for the balance injection case, the dependence of the anomalous degrdation on the electron density is estimated by the least-mean-square fitting approach. Figure 6 shows the dependece of D_{ano} against the electron density, where $D_{\mathrm{ano}} = a^2/(5.8\tau_{\mathrm{ano}})$ and $a = 0.6$ m. From the fitting, we obtain $D_{\mathrm{ano}} = 0.049 \times 10^{-19} n_e$.

By using the τ_c^{eff} from the regression, the neutron emission rate simulation is performed for the balance injection case. Figure 7 show the time evolution of the neutron emission rate for the balance injection case. Simulation results have a good agreement even for the balance injection case. From this result, the confinement degradation also occurs in the balance injection case.

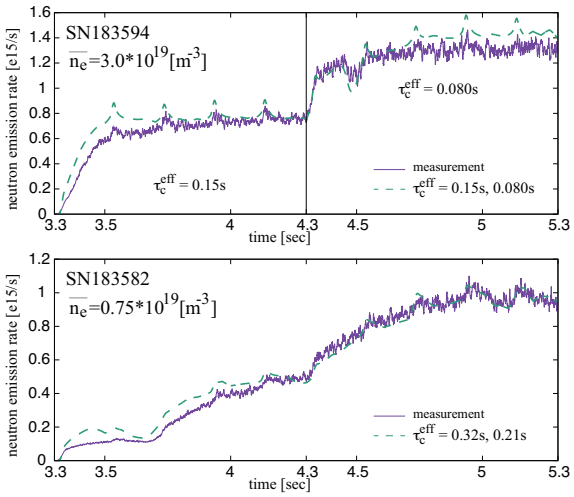

Figure 5: Time evolution of the measured and simulated neutron emission rate for the co-injection case.

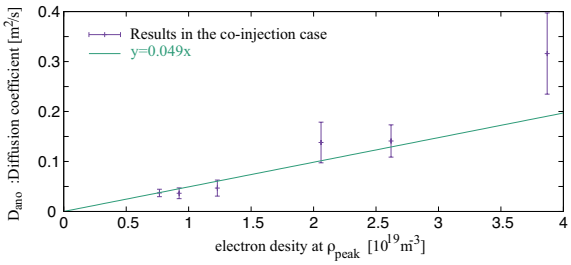

Figure 6: The particle diffusion coefficient due to the anomalous loss against the electron density.

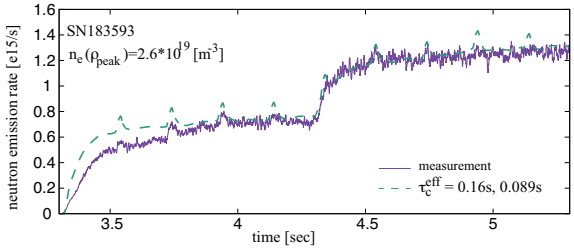

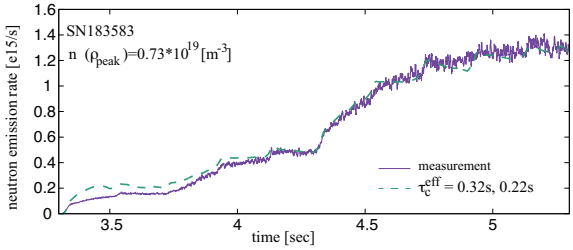

Figure 7: Time evolution of the measured and simulated neutron emission rate for the balance injection case.

Conclusion We investigated tangential NB fast-ion confinement in MHD quiescent LHD plasmas. To investigate the degradation of the fast-ion confinement, we have performed a series of experiments using deuterium gas and deuterium neutral beams in the LHD. The experimental results show that the neutron emission rate per NB power decreases as the NB power is increased in a single discharge. Because there is no significant change in the electron temperature, density, and NB shine-through rate, the reduction in the neutron emission rate per NB power indicates the degradation of the fast-ion confinement.

In this paper, we modeled the degradation to estimate the effective confinement time based on the measured data. The neutron emission rate simulation considering the confinement degradation has a good agreement with the measured neutron emission rate. Therefore, the model, including the confinement degradation depending on the NB power is valid.

Development of an adaptive predictive control system using data assimilation at LHD

Y. Morishita[1], S. Murakami[1], N. Kenmochi[2,4], H. Funaba[2], M. Yokoyama[2,4], G. Ueno[3,4,5], M. Osakabe[2,4]

[1]*Department of Nuclear Engineering, Kyoto University, Nishikyo, Kyoto, 615-8540, Japan*
[2] *National Institute for Fusion Science, National Institutes of Natural Science, Toki 509-5292, Japan*
[3]*The Institute of Statistical Mathematics, Research Organization of Information and Systems, Tokyo 190-8562, Japan*
[4]*The Graduate University for Advanced Studies, SOKENDAI, Toki 509-5292 and Tokyo 190-8562, Japan*
[5]*The Joint Support-Center for Data Science Research, Tokyo 190-0014, Japan*

1. Introduction

The operation of future fusion reactors requires a system that predicts and controls fusion plasma behavior under large uncertainties. To develop a numerical system that can control the behavior of fusion plasmas with high accuracy, we are developing a data assimilation system, ASTI [1], based on the integrated transport simulation code, TASK3D [2]. Data assimilation is a statistical method to optimize numerical simulation using observations. To realize a control system that can adapt the predictive model to the actual plasma and estimate the optimal control input based on the prediction, we have extended the data assimilation framework to include control procedures (DACS [3]) and implemented an adaptive predictive control system at the Large Helical Device (LHD) [4]. In this paper, we show the result of LHD experiments to control the central electron temperature and the issues to more advanced control experiments.

2. Data assimilation-based control system in LHD

ASTI is a data assimilation system which employs the integrated transport simulation code, TASK3D, as the system model. We have extended ASTI to a control system based on the DACS framework. ASTI assimilates the experimental time series data into the system model (TASK3D) to get the model behavior close to the actual behavior and estimate the control input for the predetermined target state using the optimized system model. ASTI can provide an adaptive model predictive control for fusion plasma.

As a first step to demonstrate the control performance of the system, we performed LHD experiments to control the central electron temperature. ASTI adjust the ECH total power to bring the central electron temperature to the target temperature. Four gyrotrons are used for the ECH; thus, ASTI controls the ECH power by selecting a subset of these four gyrotrons. ASTI sends the estimated control signals to the gyrotrons every 0.1s and assimilates the observed radial profiles of electron temperature and density every 0.3s. The radial profiles of the electron density and temperature obtained by the real-time Thomson scattering measurement system are assimilated into the system model to reduce the uncertainty in the electron and ion thermal diffusivities and improve the prediction performance of the system model.

3. Results and discussion

Figure 1 (a) shows a control result of electron temperature at the plasma center for the target temperature of 4 keV, and Fig. 1 (b) shows the adjusted ECH power. We can see that the electron temperature approaches the target temperature at 3.9 s. The control error (differences between the observed temperature and the target temperature) increases to 1 keV in the transient section (2.1-3.9 s) due to the imperfection of the system model. However, the error decreases to about 0.3 keV in the steady state section (3.9 s-). This is because the thermal diffusivity models have been adjusted to bridge the gap between the TASK3D simulation and the actual LHD plasma in the adaptation step.

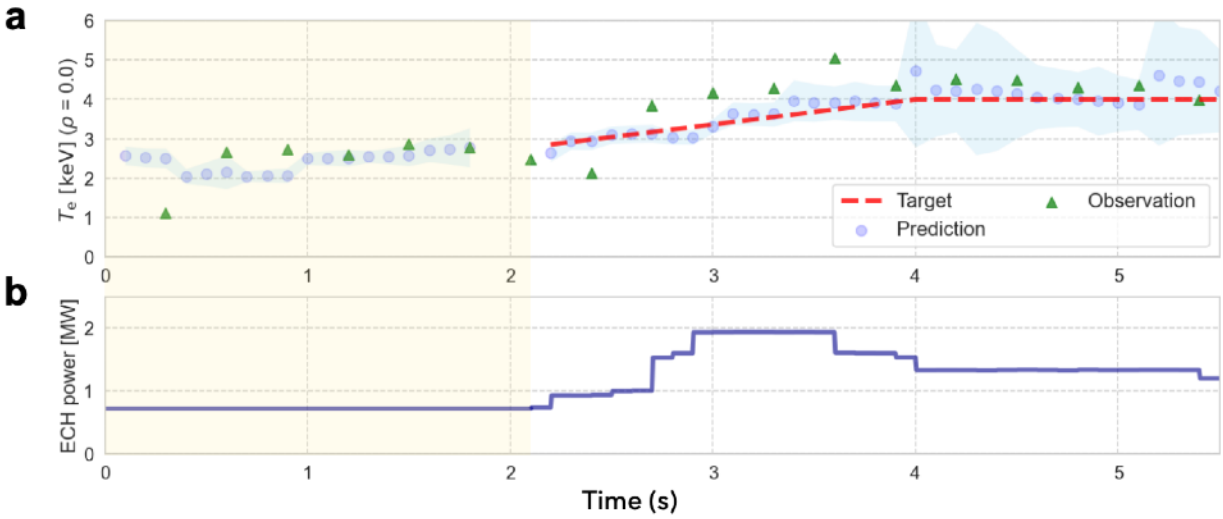

Fig. 1 Results of a control experiment (#186502). (a) Control result of the electron temperature at the plasma center. (b) Adjusted ECH power by ASTI. The blue hatching areas represent the one standard deviation of the predicted distribution.

We must address the following issues for more advanced experiments in the future.

- To prevent a reduction in the control performance due to delays in adaptation, we require a control algorithm that reflects observed information into the prediction and control estimation more quickly.
- The probability distribution of model parameters should be adjusted by considering the physical characteristics and control accuracy to avoid control instability.
- Reduction of the control error in the transient phase makes it necessary to improve the assumed transport model.

References

[1] Y. Morishita, *et al*., Computer Physics Communications **274**, 108287 (2022).
[2] S. Murakami, *et al*., Plasma Phys. Control. Fusion **57**, 119601 (2015).
[4] Y. Morishita, *et al*., J. Computational Science **72**, 102079 (2023).
[5] Y. Morishita, *et al*., Scientific Reports **14**, 137 (2024).

Study of model-based control for tokamak plasma profile

M. Sato[1], M. Kishida[1,2], S. Sakakibara[1,3], *M. Yokoyama[1,3]
[1]SOKENDAI, [2]National Institute of Informatics, [3]National Institute for Fusion Science

1. Introduction

Controlling the plasma profile remains a significant challenge in achieving a fusion reactor. To control highly autonomous complex dynamics, such as burning plasmas, conventional PID control mechanisms are inadequate. Therefore, we are seeking ways to control the plasma profile from the viewpoint of control theory and aim to develop more advanced control methods.

2. What is control theory?

Control theory is the study of systems that have inputs and outputs, and it involves modeling, analyzing, and finally designing controllers.

The first step in controller design is modeling. There are three main methods of modeling: first-principles modeling, black box modeling, which only uses the relationship between inputs and outputs, and grey box modeling. System models are typically defined using **state equations**. It is expressed as follows:

$$\dot{\boldsymbol{x}} = \boldsymbol{f}(\boldsymbol{x}, \boldsymbol{u}) \quad \textbf{(1)}$$
$$\boldsymbol{y} = \boldsymbol{g}(\boldsymbol{x}, \boldsymbol{u}) \quad \textbf{(2)}$$

where $x \in \mathbb{R}^n$ is state vector, $u \in \mathbb{R}^r$ is input vector and $y \in \mathbb{R}^q$ is output vector. There are different ways to express the state equation, including **linear time-invariant systems (LTIs)**, **nonlinear systems**, etc.

The second step is system analysis. System stability analysis is an essential aspect that needs to be given special attention. This is because the major purpose of control is to stabilize the system.

The last step is "**tools"** selection. Control theory encompasses various tools, such as Robust control theory which considers model uncertainty, and Optimal control theory which deals with constraints. When designing controllers, several tools can be used for various purposes.

3. Plasma profile control model

Plasma profile control models have been developed globally using different approaches. For example, a 1D diffusion-like parabolic equation for the radial profile of the plasma poloidal flux or current density. Readers could refer to Witrant et al. [2007]. This is a control model known as a distributed parameter system in control theory. It requires advanced mathematical understanding. Another example is a port-Hamiltonian system for plasma profile which is referred to in Vu [2012]. A port-Hamiltonian system is a framework used in physics and control theory to model and analyze complex dynamical systems. Various profile control experiments are being conducted around the world using these control models.

4. Prospects for future studies

To control complex systems, advanced control logic is required; particularly, the port-Hamiltonian formulation of burning plasma will be studied intensively for future studies. In recent years, there have been many data science approaches, including AI. However, it is always necessary to have a control theory framework when discussing system stability and other issues. In fact, since various instabilities exist in plasmas, such as MHD instability, it is crucial to control these instabilities. A comprehensive understanding of various factors and plasma control is essential to realize future fusion reactors. Model-based control is a promising solution.

5. References

[1] Witrant, E., Joffrin, E., Brémond, S., Giruzzi, G., Mazon, D.,Barana, O., and Moreau, P. (2007). A control-oriented model of the current profile in tokamak plasma. Plasma Phys. Control.Fusion, 49, 1075–1105.

[2] Vu, NM., Lefevre, L., Maschke, B. (2012). Port-Hamiltonian formulation for systems of conservation laws: application to plasma dynamics in Tokamak reactors. IFAC Proceedings Volumes Volume 45, Issue 19, 2012, Pages 108-113

Prediction of radiative collapse by analyzing videos of plasma discharge with CNN in LHD

Yuya Suzuki[1], Mamoru Shoji[1,2], Naoki Kenmochi[1,2], and Masayuki Yokoyama[1,2]

[1]SOKENDAI, [2]National Institutes of Natural Sciences, National Institute for Fusion Science

1. Introduction

The unexpected termination of plasma discharges has been a critical issue for nuclear fusion research. One of the termination events observed in the Large Helical Device (LHD) is named “radiative collapse”. This event occurs in the plasma edge region and is caused by impurity influx, which cools down the plasma temperature with strong luminescent light and prevents the sustainment of high-density plasmas [1]. To avoid this event, a new method that predicts the radiative collapse from the images of plasma discharges is proposed using Convolutional Neural Networks (CNN) which is one of the machine learning models.

2. Dataset for training model

To train a model on features of radiative collapse, a dataset was created from discharges with radiative collapse. The search was conducted using experimental data with a magnetic axis of 3.6 m, a magnetic field of 2.75 T, and shot numbers ranging from 157000 to 162000 with hydrogen as the fuel. As a result, 41 discharges were selected. From plasma discharges video of these discharges, images of stable and collapse state were extracted and labeled. These images were used for dataset.

3. Accuracy evaluation of trained determination models

A CNN model called EfficientNet[2] was used to determine the discharge state from the images. The training results of the model for each camera are shown in figure 1. Except for a few cameras, the accuracy during training, accuracy on the evaluation dataset and F-score were all above 86%. This result shows that the models in those cameras were successfully trained and a determination model with high accuracy was obtained.

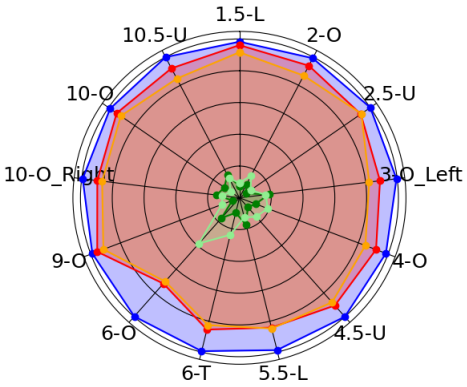

Fig 1. Results of trained models at various evaluation parameters. Outer labels show camera's name.
Learning : Accuracy on the training dataset
Demo : Accuracy on the evaluation dataset
F score : Accuracy considering data bias
Miss : Misjudged images in collapse state
False : Misjudged images in stable state.

4. Performance of determination models as predictor

The determination model was applied to a plasma discharge video as a predictor. The results are shown in Figure 2. The blue hatched area is the area defined as stable, so models with a collapse judgement from this section are excluded. As a result, models such as 10-O and 2-O were able to predict about 2-4 frames (66-132 milliseconds) before the radiative collapse.

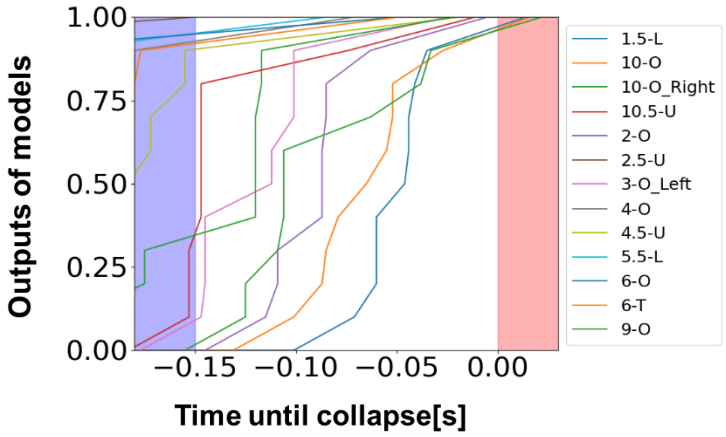

Fig 2. Average output of the discharge state determination model and time to onset of radiative collapse at the point of output.

5. Analysis of the focus area of the determination models

The determination basis of the model was visualized by a method called GradCAM[3]. The results are shown in Figure 3. The results show that there were two main determination patterns of the model: one was the emission of plasma near the divertor tiles, and the other was the transparency of the plasma. As these features are areas that have been mentioned in previous studies [1], it was found that the model focused on significant areas in the image to determine.

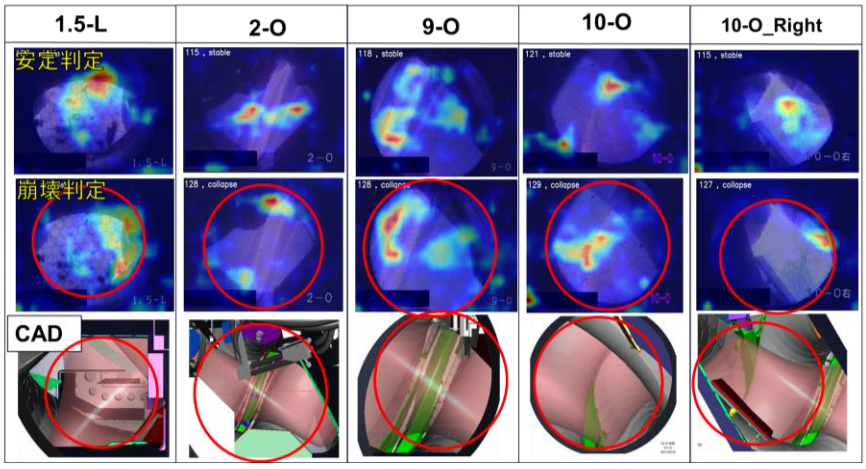

Fig 3. Heat map showing the area of interest for the discharge state determination model by GradCAM.

6. Conclusion

A discharge state discrimination model could be created by using camera images accumulated from previous plasma discharge experiments at LHD for machine learning. For the cameras with good accuracy, the determination accuracy of the images was about 86-92% and the prediction performance was about 2-4 frames, which was sufficient for predictive control. These models were also found to determine from areas in the image that captured phenomena such as those mentioned in previous studies. The results demonstrate the effectiveness of machine-learning-based controllers and data-driven research in plasma and fusion research.

7. Reference

[1] B.J. Peterson, *et al*., Plasma Fusion Res. **1**, 045, (2006).
[2] Mingxing Tan and Quoc V.Le, arXiv:1905.11946 (2019)
[3] Selvaraju R.R., *et al.*, arXiv:1610.02391 (2016)

Introduction of hydrogen isotope effects to a turbulent transport model DeKANIS and its application to integrated simulations

E. Narita[1], M. Honda[1], M. Nakata[2,3], N. Aiba[4], N. Hayashi[4], T. Nakayama[3], and M. Yoshida[4]

[1]Graduate School of Engineering, Kyoto University, Kyoto, Japan
[2]National Institute for Fusion Science, Gifu, Japan
[3]The Graduate University for Advanced Studies, Gifu, Japan
[4]National Institutes for Quantum Science and Technology, Ibaraki, Japan

1 Introduction

Hydrogen isotope effects are crucial in predicting burning plasma performance with the knowledge of physics in deuterium and hydrogen plasmas. Experimental observations show positive isotope effects in several devices (see e.g. [1,2]), and several factors have been reported with gyrokinetic codes to explain the experiments (see e.g. [3,4]). In this study, we have introduced hydrogen isotope effects into a turbulent transport model DeKANIS [5] and performed temperature and density profile predictions with the modified model.

2 How to introduce the hydrogen isotope effects into DeKANIS

DeKANIS calculates the electron particle and heat fluxes with the following expressions: $\bar{\Gamma}_\mathrm{e} = \bar{D}\left(\frac{R}{L_{n_\mathrm{e}}} + C_\mathrm{T}\frac{R}{L_{T_\mathrm{e}}} + C_\mathrm{P}\right)$ and $\bar{Q}_\mathrm{e} = \bar{\chi}_\mathrm{e}\left(C_\mathrm{N}\frac{R}{L_{n_\mathrm{e}}} + \frac{R}{L_{T_\mathrm{e}}} + C_\mathrm{HP}\right)$. Here, non-dimensional $\bar{D}$, $\bar{\chi}$, R/L_n and R/L_T are the particle and heat diffusivities and the normalized density and temperature gradients, respectively. The fluxes consist of the diagonal and off-diagonal terms, which are quantitatively determined by estimating the off-diagonal term coefficients ($C_\mathrm{T,P,N,HP}$) and the diffusivities ($\bar{D}$ and $\bar{\chi}_\mathrm{e}$). DeKANIS also predicts the ion heat flux, which is given as $\bar{Q}_\mathrm{i} = \frac{\bar{\chi}_\mathrm{i,eff}}{\bar{\chi}_\mathrm{e,eff}}\bar{\chi}_\mathrm{e,eff}\frac{R}{L_{T_\mathrm{i}}}\frac{n_\mathrm{i}}{n_\mathrm{e}}\frac{T_\mathrm{i}}{T_\mathrm{e}}$. Here, $\bar{\chi}_\mathrm{eff}$ is the normalized effective heat diffusivity. Once $\bar{\chi}_\mathrm{e,eff}$ is obtained with $\bar{Q}_\mathrm{e}$, $\bar{Q}_\mathrm{i}$ can be calculated by determining $\bar{\chi}_\mathrm{i,eff}/\bar{\chi}_\mathrm{e,eff}$. To forecast $\bar{\Gamma}_\mathrm{e}$, $\bar{Q}_\mathrm{e}$ and $\bar{Q}_\mathrm{i}$, DeKANIS utilizes a neural network (NN) model and a saturation model. The NN model is trained to evaluate $C_\mathrm{T,P,N,HP}$ and $\bar{\chi}_\mathrm{i,eff}/\bar{\chi}_\mathrm{e,eff}$, whose training datasets are prepared by the linear gyrokinetic calculations with GKW [6] at the normalized wavenumber $\bar{k}_\theta$ where the normalized linear growth rate takes the maximum value, $\bar{\gamma}_\mathrm{max}$, of the ion temperature gradient (ITG) mode or the ITG/trapped electron mode (TEM). The NN model also outputs the corresponding $\bar{k}_{\theta,\bar{\gamma}_\mathrm{max}}$ and $\bar{\gamma}_\mathrm{max}$, which are passed to the saturation model to determine $\bar{D}$. The remaining coefficient, $\bar{\chi}_\mathrm{e}$, is calculated with the relationship between $\bar{D}$ and $\bar{\chi}_\mathrm{e}$: $\bar{\chi}_\mathrm{e} = \bar{D}(C_\mathrm{T} + 1.5)/C_\mathrm{N}$.

The previous training datasets of the NN models were given only by the calculations assuming deuterium plasmas. To consider the changes in the output parameters due to the main ion mass m_i, we have introduced m_i as an input parameter and added the calculations assuming hydrogen and tritium plasmas to the training datasets. The saturation model has also been modified

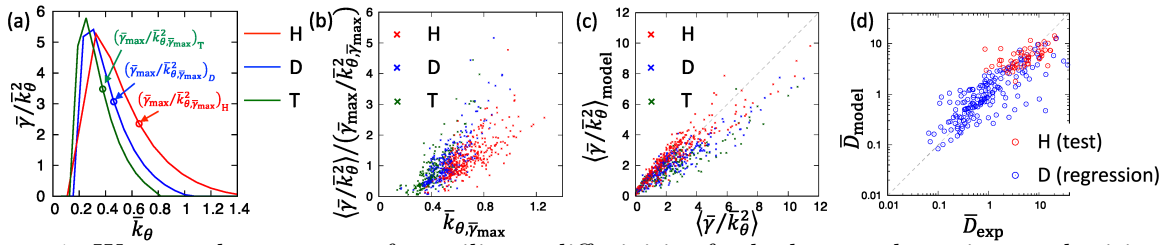

Figure 1. Wavenumber spectra of quasilinear diffusivities for hydrogen, deuterium and tritium plasmas. The circles denote the quasilinear diffusivities at the wavenumber where the linear growth rate takes the maximum value. (b) The ratio of the wavenumber integral of the quasilinear diffusivity to the quasilinear diffusivity at the wavenumber where the linear growth rate takes the maximum value as a function of the wavenumber. (c) Comparison of the wavenumber integral of the quasilinear diffusivity and its model. (d) Comparison of the semi-empirically estimated particle diffusivity and its model for hydrogen and deuterium plasmas.

founded on the hydrogen isotope effects given by linear gyrokinetic calculations. The details of the new saturation model is shown in the next section.

3 Modification of the saturation model

The new saturation model includes the two kinds of hydrogen isotope effects. The first one is the difference in the suppression of the TEM due to collisions depending on m_i [4]. When we perform linear gyrokinetic calculations and compute the quasilinear diffusivity $\bar{\gamma}/\bar{k}_\theta^2$ as a function of $\bar{k}_\theta$ like in Fig. 1(a), the wavenumber integral of $\bar{\gamma}/\bar{k}_\theta^2$ can be estimated as a proxy of a diffusivity given by a nonlinear calculation. Here, the wavenumber integral of $\bar{\gamma}/\bar{k}_\theta^2$ is defined as $\langle\bar{\gamma}/\bar{k}_\theta^2\rangle = \left[\sum_{\bar{k}_\theta}\left(\bar{\gamma}/\bar{k}_\theta^2\right)\Delta\bar{k}_\theta\right]/\bar{k}_{\theta,\mathrm{lim}}$, where $\Delta\bar{k}_\theta$ is the interval of $\bar{k}_\theta$ used for the calculation and $\bar{k}_{\theta,\mathrm{lim}}$ is the upper limit of the integration. In this study, $\bar{k}_\theta$ and $\bar{\gamma}$, are normalized with the deuterium unit. Since the TEM is more suppressed for the heavier ion mass case due to collisions [4], $\langle\bar{\gamma}/\bar{k}_\theta^2\rangle$ decreases with the increase in m_i as found in Fig. 1(a). The second hydrogen isotope effect is the change in the residual zonal flow level. When we perform linear gyrokinetic calculations, a reduction in the residual zonal flow level with an increase in the collision frequency is found. This tendency can be expected by [7], where the suppression of turbulence by zonal flows considering collisional decay is given as $\nu_\mathrm{f}^2/\omega_\mathrm{f}^4 + K_\mathrm{RH}^2\tau_\mathrm{c}/\nu_\mathrm{d}$. Here, $\omega_\mathrm{f} = v_\mathrm{th,i}/R$, $\nu_\mathrm{f} = \omega_\mathrm{f}\exp\left(-q^2\right)$, K_RH is the linear zonal flow response function without collisions [8], τ_c is the correlation time and $\nu_\mathrm{d} = 0.67/\left(\tau_\mathrm{ii}\epsilon\right)$ with the ion thermal velocity $v_\mathrm{th,i}$, the major radius R, the safety factor q, the inverse aspect ratio ϵ and ion-ion collision time τ_ii. A square root of $\nu_\mathrm{f}^2/\omega_\mathrm{f}^4 + K_\mathrm{RH}^2\tau_\mathrm{c}/\nu_\mathrm{d}$, which is defined as characteristic time of the residual zonal flow, τ_r, in this study, is found to be proportional to $m_\mathrm{i}^{0.5}$.

The second hydrogen isotope effect can be included by introducing τ_r to the saturation model, but the inclusion of the first one requires a model that expresses $\langle\bar{\gamma}/\bar{k}_\theta^2\rangle$ with $\bar{k}_{\theta,\bar{\gamma}_\mathrm{max}}$ and $\bar{\gamma}_\mathrm{max}$. $\bar{k}_{\theta,\bar{\gamma}_\mathrm{max}}$ tends to be lower for the heavier ion mass case, and $\bar{\gamma}_\mathrm{max}/\bar{k}_{\theta,\bar{\gamma}_\mathrm{max}}^2$ often does not reflect the tendency of $\langle\bar{\gamma}/\bar{k}_\theta^2\rangle$ as shown with the circles in Fig. 1(a). The relationship between $\langle\bar{\gamma}/\bar{k}_\theta^2\rangle$ and $\bar{\gamma}_\mathrm{max}/\bar{k}_{\theta,\bar{\gamma}_\mathrm{max}}^2$ was investigated by performing linear calculations with different m_i for a variety of plasma parameters with $\bar{k}_{\theta,\mathrm{lim}} = 1.2$, and it was found that $\langle\bar{\gamma}/\bar{k}_\theta^2\rangle/(\bar{\gamma}_\mathrm{max}/\bar{k}_{\theta,\bar{\gamma}_\mathrm{max}}^2)$ increases with $\bar{k}_{\theta,\bar{\gamma}_\mathrm{max}}$ as shown in Fig. 1(b). This trend can be expressed with the following functional formula: $\langle\bar{\gamma}/\bar{k}_\theta^2\rangle_\mathrm{model} \sim \mathrm{coef}\left(\bar{\gamma}_\mathrm{max}/\bar{k}_{\theta,\bar{\gamma}_\mathrm{max}}^2\right)\left(\bar{k}_{\theta,\bar{\gamma}_\mathrm{max}}/\bar{k}_{\theta,\mathrm{lim}}\right)^\alpha$. coef and α were determined by regression analysis utilizing the calculation results shown in Fig. 1(b) as coef $= 3.01$ and $\alpha = 1.33$, and the obtained model can express $\langle\bar{\gamma}/\bar{k}_\theta^2\rangle$ for all hydrogen isotope species (Fig. 1(c)).

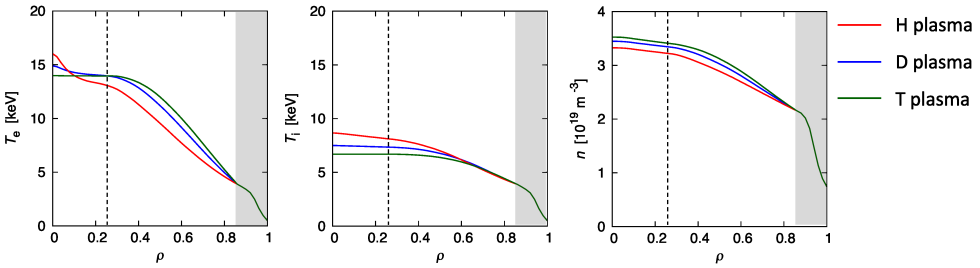

Figure 2. Radial profiles of the electron and ion temperatures and the electron density predicted by the transport simulation with TOPICS for ITER PFPO-1 relevant plasmas, with the change in the main ion mass.

The new saturation model was obtained as $\bar{D} = 1.23\langle\bar{\gamma}/\bar{k}_\theta^2\rangle_{\rm model}^{0.752}\left[0.1\bar{\tau}_{\rm r}\langle\bar{\gamma}/\bar{k}_\theta^2\rangle_{\rm model}^{0.5}\right]^{1.20}$. The constant 0.1 in the zonal flow part adjusts its order. The constant 1.23 and the exponents were determined by regression analysis to reproduce the semi-empirically estimated particle diffusivity $\bar{D}_{\rm exp}$. Although $\bar{D}_{\rm exp}$ was estimated based on electron heat fluxes of JT-60U deuterium plasmas, the obtained saturation model can express $\bar{D}_{\rm exp}$ for both the deuterium cases used for the regression analysis and the hydrogen cases introduced as test cases as shown in Fig. 1(d). Therefore, the saturation model could be used also for tritium plasmas.

4 Integrated simulations including the hydrogen isotope effects

The modified DeKANIS was implemented in the integrated code TOPICS [9] and temperature and density predictions were performed for plasmas envisioned in the ITER pre-fusion power operation 1 (PFPO-1) phase with three cases having different main ion species: hydrogen, deuterium and tritium, as shown in Fig. 2. Here, the magnetic equilibrium and the pedestal height are fixed, the plasma current is 5.0 MA, the toroidal magnetic field is 1.8 T and the electron cyclotron heating power is 30 MW. The electron temperature and density are higher for the heavier ion mass case, but the ion temperature is higher for the lighter ion mass case. The change in the electron profiles should be caused by the reduction in the diffusivities with the increase in $m_{\rm i}$, and that in the ion one may be due to the collisional equipartition, which is larger for the lighter ion mass case. The thermal energy confinement time is 2.15, 2.34 and 2.42 for the hydrogen, deuterium and tritium cases, respectively. The predicted dependence of the thermal energy confinement time on $m_{\rm i}$ is weaker than that of the scaling the IPB98(y,2) scaling. It may be due to the same pedestal height for the three cases. We will develop a pedestal model including hydrogen isotope effects in the future.

References

[1] H. Urano *et al.,* Nucl. Fusion **53** 083003 (2013).
[2] C.F. Maggi *et al.,* Plasma Phys. Control. Fusion **60** 014045 (2018).
[3] J. Garcia *et al.,* Plasma Phys. Control. Fusion **64** 054001 (2022).
[4] M. Nakata *et al.,* Phys. Rev. Lett. **118** 165002 (2017).
[5] E. Narita *et al.,* Contrib. Plasma Phys. e202200152 (2023).
[6] A.G. Peeters *et al.,* Comput. Phys. Commun. **180** 2650 (2009).
[7] F.L. Hinton and M.H. Rosenbluth, Plasma Phys. Control. Fusion **41** A653 (1999).
[8] M.N. Rosenbluth and F.L. Hinton, Phys. Rev. Lett. **80** 724 (1998).
[9] N. Hayashi and JT-60 Team, Phys. Plasmas **17** 056112 (2010).

Research of turbulent transport due to dissipative trapped electron mode in tokamak plasmas

S. Toda[1,2], M. Nunami[1,3], and N. Kasuya[4]
[1]*National Institute for Fusion Science*
[2]*Graduate Institute for Advanced Studies, SOKENDAI*
[3]*Graduate School of Science, Nagoya University*
[4]*Research Institute for Applied Mechanics, Kyushu University*

Turbulent transport is one of the most important subjects in research of toroidal plasmas. The purpose of this study is to quantify turbulent transport. Microscopic plasma instabilities are studied using electromagnetic gyrokinetic simulations. The trapped electron mode (TEM) where normalized electron collision frequency is less than unity[1] is called dissipative-TEM in a high collisional regime. Here, this mode is driven by dissipation from the electron collision and ions do not need to be in the banana regime. This mode is known to be driven unstable in the presence of density and/or temperature gradients. Plasma experiments at the PLATO device at the Research Institute for Applied Mechanics, Kyushu University have been started. Transport simulations using integrated code are carried out on the PLATO tokamak to forecast plasma performance and plasma profiles in the PLATO are predicted using an empirical model in the integrated code, the TASK code. In these plasmas, the electron collision frequency is typically less than the electron bounce collision frequency and the ion collision frequency is larger than the ion bounce collision frequency. Therefore, these plasmas are in a high collisional regime and the d-TEM is predicted to be unstable. We focus on the d-TEM and the ITG mode by using local gyrokinetic simulations. The GKV code[2] is used for local flux tube gyrokinetic simulation, using the Sugama collision model operator[3] or the Lenard-Bernstein collision model operator. The Sugama collision operator was used to study the linear response of the zonal flows with a collisional effect[4]. In these analysis results, the residue level of the zonal flows using the Sugama collision operator was found to be close to the analytically predicted one. On the other hand, the linear response of the zonal flows using the Lenard-Bernstein collision operator shows over-damping. Therefore, the Sugama collision model operator is used for the local gyrokinetic simulation in this study.

The plasma profiles predicted by the TASK code in the PLATO are used. The linear simulation results using the Sugama (S) and Lenard-Bernstein (LB) collision operators are compared. The linear growth rate is studied at $k_x\rho_\mathrm{e} = 0.0$ and in $0.0 \leq k_y\rho_\mathrm{e} \leq 0.06$ region, where k_x and k_y are the radial and poloidal wavenumbers, respectively. The dependences of linear growth rate γ, and real angular frequencies ω, on the normalized poloidal wavenumber $k_y\rho_\mathrm{e}$, are studied. The linear growth rate γ, and the real angular frequencies ω, as the function of $k_y\rho_\mathrm{e}$ are also investigated. Using the S collision operator, the instabilities predicted in this study are driven by the d-TEM in the regions $0.005 \leq k_y\rho_\mathrm{e} \leq 0.020$ at $\rho = 0.47$ and $0.005 \leq k_y\rho_\mathrm{e} < 0.040$ at $\rho = 0.65$. The real angular frequency changes from the electron to ion diamagnetic drift motion direction at $\rho = 0.47$ and $\rho = 0.65$ when the poloidal wavenumber increases. The so-called d-TEM is unstable, where the electron collision frequency is less than the electron bounce frequency and the ion collision frequency is larger than the ion bounce frequency[1]. This d-TEM is driven by the density gradient in this study. The d-TEM is predicted to be unstable at $\rho = 0.81$ in the all-poloidal wavelength region studied here. The linear growth rate for the d-TEM at $\rho = 0.81$ becomes larger than that at $\rho = 0.47$ because of the increase of R/L_n, therefore, the d-TEM becomes more unstable in the outer radial region. On the other hand, the ITG mode is excited in the regions $0.020 < k_y\rho_\mathrm{e} < 0.060$ at $\rho = 0.47$ and $0.040 \leq k_y\rho_\mathrm{e} < 0.060$ at $\rho = 0.65$. The ITG is stable at $\rho = 0.81$ because R/L_{T_i} is smaller than that at $\rho = 0.47$ or $\rho = 0.65$. The rapid changes from the d-TEM to the ITG mode are obtained in the dependence of the real angular frequency on the poloidal wavenumber, specially at $\rho = 0.65$. Using the LB collision operator, only the d-TEM is unstable in the $0.005 < k_y\rho_\mathrm{e} < 0.030$

region at all radial points. The differences between the results using S and LB collision operators are found. These are because the field particle part is included with momentum conservation and the collisionality term depends on the velocity in the S collision model operator[3,4].
Next, we study the linear response of the zonal flows using the S and LB model collision operators. The zonal flow decay time[5] is investigated by the linear gyrokinetic simulation results. We examine the linear response of the zonal flows using S and LB collision operators. Here, the linear response function of zonal flows $\mathcal{R}_{\tilde{k}_x}(t)$ is defined as $\mathcal{R}_{\tilde{k}_x}(t) = \left\langle \tilde{\phi}_{\tilde{k}_x,\tilde{k}_y=0}(t) \right\rangle / \left\langle \tilde{\phi}_{\tilde{k}_x,\tilde{k}_y=0}(t=0) \right\rangle$, where $\tilde{\phi}(= \phi/(T_{\rm e}\rho_{\rm e}/(eR)))$ is the electrostatic potential fluctuation. We set $\tilde{k}_x = 0.01$. The residue levels at $\rho = 0.47$, $\rho = 0.65$ and $\rho = 0.81$, which is defined as the value of $\mathcal{R}_{\tilde{k}_x}(t = 2500)$ here, are studied. The residue level using the S collision operator is larger than that using the LB one. The zonal flow decay time is defined as $\int_0^{2500} \mathcal{R}_{\tilde{k}_x}(t)dt$ in this article. The zonal flow decay time is also studied. The zonal flow decay time using the S collision operator is found to be twice as large as that using the LB collision operator. The linear simulation results suggest that the effect of the zonal flows on the turbulent transport using the S collision operator in the nonlinear simulation results is larger than that using the LB collision operator.
A nonlinear gyrokinetic simulation is carried out. A nonlinearly saturated state for plasma turbulence is obtained. Nonlinear gyrokinetic analysis results are studied for the time evolutions of the squared turbulent potential fluctuation, $\mathcal{T}\left(= \Sigma_{\tilde{k}_x,\tilde{k}_y\neq 0} \left\langle |\tilde{\phi}_{\tilde{k}_x,\tilde{k}_y}|^2 \right\rangle /2\right)$ and the squared zonal flow potential, $\mathcal{Z}\left(= \Sigma_{\tilde{k}_x,\tilde{k}_y=0} \left\langle |\tilde{\phi}_{\tilde{k}_x,\tilde{k}_y}|^2 \right\rangle /2\right)$. Time evolutions for the squared potential fluctuations using the S and LB collision model operators are compared at $\rho = 0.47$, $\rho = 0.65$ and $\rho = 0.81$. To study the effect of the zonal flows, the values of $\bar{\mathcal{T}}$ and $\bar{\mathcal{Z}}$ at $\rho = 0.47, 0.65$ and 0.81 are examined. The symbol $\bar{}$ represents the averaged values of $\mathcal{T}$ or $\mathcal{Z}$ of time t normalized by $R/v_{\rm te}$ from 3000 to 5000. The effect of the zonal flows on the turbulence by the S collision operator is predicted to be much larger than that by the LB one. The values of $\bar{\mathcal{Z}}/\bar{\mathcal{T}}$ at $\rho = 0.47, 0.65$ and 0.81 using the S and LB collision model operators are studied. The values of $\bar{\mathcal{Z}}/\bar{\mathcal{T}}$ using the S collision model operator are larger than those using the LB collision model operator. Next, the transport level is evaluated by the nonlinear simulation results. The averaged values over the time interval after the nonlinear saturation for $Q_{\rm e}$, $\chi_{\rm e}$, $Q_{\rm i}$, $\chi_{\rm i}$, Γ and D using the S and LB collision model operators are obtained, where Q_j is the energy flux and χ_j is the energy diffusivity for the species j. Here, Γ is particle flux and D is particle diffusivity. The normalized values of $Q_{\rm e}/Q_{\rm e}^{\rm GB}$, $\chi_{\rm e}/\chi_{\rm e}^{\rm GB}$, $Q_{\rm i}/Q_{\rm e}^{\rm GB}$, $\chi_{\rm i}/\chi_{\rm e}^{\rm GB}$, $\Gamma/\Gamma^{\rm GB}$ and $D/\chi_{\rm e}^{\rm GB}$ using the S and LB collision model operators are also obtained. Energy and particle fluxes at $\rho = 0.47, 0.65$ and 0.81 are studied. The energy and particle diffusivities at $\rho = 0.47, 0.65$ and 0.81 are indicated. The energy and particle fluxes normalized by the gyro-Bohm unit at $\rho = 0.47, 0.65$ and 0.81 are also studied. The energy and particle diffusivities normalized by the gyro-Bohm unit at $\rho = 0.47, 0.65$ and 0.81 are also investigated. The transport levels using the S collision model operator are found to be smaller than those using the LB one except in the case of electron energy transport at $\rho = 0.81$ due to the effect of the zonal flows.

REFERENCES

[1]B. B. Kadomtsev and O. P. Pogutse, *Reviews of Plasma Physics, edited by M. Leontovich*, Vol. 5 (consultants Bureau, New York, 1970).
[2]T.-H. Watanabe and H. Sugama, Nucl. Fusion **46**, 24 (2006).
[3]H. Sugama, T. H. Watanabe, and M. Nunami, Phys. Plasmas **16**, 112503 (2009).
[4]M. Nunami, M. Nakata, T. H. Watanabe, and H. Sugama, Plasma and Fusion Research **10**, 1403058 (2015).
[5]S. Ferrando-Margalet, H. Sugama, and T.-H. Watanabe, Phys. Plasmas **14**, 122505 (2007).

統合乱流計測シミュレータの開発とそのトーラス装置計測への応用

Development of Integrated Turbulence Diagnostic Simulator and Its Application to Torus Device Measurements

N. Kasuya[1,2], R. Yoshihara[2], T. Ido[1,2], M. Nunami[3], K. Tanaka[1,3], S. Satake[3], K. Fujita[4], M. Yagi[5]

[1]RIAM, Kyushu University, Kasuga, Fukuoka, Japan

[2]IGSES, Kyushu University, Kasuga, Fukuoka, Japan

[3]National Institute for Fusion Science, Toki, Gifu, Japan

[4]Gradutae School of Science, Nagoya University, Nagoya, Aichi, Japan

[5]National Institute for Quantum and Radiological Science and Technology, Rokkasho, Aomori, Japan

E-mail: kasuya@riam.kyushu-u.ac.jp

1. Introduction

Plasma turbulence has large effects on particle and heat transport in magnetically-confined fusion plasmas, and it is important to clarify its 3-D feature in real magnetic geometries in torus experiments, because various global and meso-scale structures are formed. Synthetic diagnostics use simulation data to represent experimental measurements by simulating measurement signals [1-5]. Numerical simulations can show global features of mean profile modifications and fluctuation excitations, and quantitative comparison between experiments and simulations is possible. We have been carrying out some numerical diagnostics for turbulence and structural formation analyses [6,7]. On the other hand, several kinds of simulations use different models, depending on the simulation targets, so comparison between models is also important to capture various characteristics in magnetized plasmas. In addition, combination of multiple simulation results can give complex plasma characteristics including several physical mechanisms. Therefore, we newly develop these analysis routines into an integrated numerical diagnostic platform for multiple simulation data [8].

2. Integrated turbulence diagnostic simulator

The integrated turbulence diagnostic simulator (iTDS) is a framework for making global analyses in real magnetic geometries of fusion devices [8,9]. iTDS connects global simulations and experimental observations. Various analysis routines for several experimental diagnostics are developed on this platform. The analysis consists of the following processes;

i) 3-D simulation of plasma instabilities and transport

ii) Plasma device parameter set and adjustment of the data format (if necessary)

iii) Simulation to obtain signals by experimental diagnostics

In process i), several codes can be used to obtain 3-D plasma profiles and time evolution of fluctuations. Global codes are used for calculations in torus plasma geometries. In general, particular models do not always include all the necessary quantities, so lacked information is supplemented with other calculation or assumption, if necessary in process ii). In addition, spatial coordinates in simulation codes may be different with ones used for numerical measurement, so data transfer is necessary in that case. Data mapping to the common format is often used, but here we introduce the object-oriented method in accordance with each data format to gain the maximum information. The data transfer is limited to the minimum. Then the numerical measurements are carried out in process iii). The basic component to capture

3-D dynamics from simulation data is extracting the local value at the arbitrary position from discreet data by interpolation. The combination of this basic routine can give multi-point observation along a line of the sight of each diagnostic. Here the focus is mainly set on a geometric effect from magnetic configurations. Applications of iTDS is explained in the followings to show mean profile and fluctuation measurements in torus experimental devices.

3. Steady profile measurement

HIBP is powerful diagnostic to give information of several kinds of quantities [10]. Single trajectory of the detected ion can be selected with given injection and detection conditions, which determines the observation position. Plasma fluctuations and electromagnetic fields inside the plasma can be measured simultaneously without disturbing the plasma. Calculation of 3-D trajectory of heavy ions, including non-circular plasma shape and experimental arrangement of diagnostics, is carried out by synthetic HIBP (sHIBP) in iTDS for LHD. The following set of equations of motion in cylindrical coordinates (R, ϕ, z) is used for the calculations;

$$\ddot{R} = R\left(\dot{\phi}\right)^2 - \frac{q}{m}\frac{\partial \Phi}{\partial R} + \frac{q}{m}\left(R\dot{\phi}B_z - \dot{z}B_\phi\right) \qquad (1a)$$

$$\ddot{\phi} = -2\frac{1}{R}\dot{R}\dot{\phi} - \frac{q}{m}\frac{1}{R^2}\frac{\partial \Phi}{\partial \phi} + \frac{q}{m}\frac{1}{R}\left(\dot{z}B_R - \dot{R}B_z\right) \qquad (1b)$$

$$\ddot{z} = -\frac{q}{m}\frac{\partial \Phi}{\partial z} + \frac{q}{m}\frac{1}{R}\left(\dot{R}B_\phi - R\dot{\phi}B_R\right) \qquad (1c)$$

Mean radial Φ_0 and 3-D perturbation Φ_1 profiles of the potential are included in the 3-D magnetic configurations with (B_R, B_ϕ, B_z). The 3-D variation of the potential is calculated by global drift kinetic code FORTEC-3D, which is given by the neoclassical process [11]. This 3-D variation is predicted to affect the impurity neoclassical transport. An example of the calculated trajectories of the injected heavy ions are shown in Fig. 1 with their ionization points from charge number +1 to +2, which are the observation points for HIBP. For the calculations, it is necessary to use magnetic fields for the whole regions inside and outside of the last closed flux surfaces (LCFS). The magnetic fields generated by external coils (vacuum fields) are modified to be equilibrium fields in the plasma discharges. FORTEC 3-D solves the set of equations by using magnetic fields from equilibrium code VMEC [12] only inside

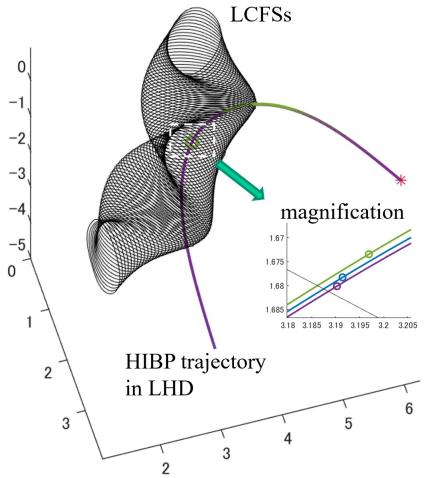

FIG. 1. HIBP trajectory from the injection point to the detection point in the vacuum vessel. Three cases are indicated with usage of (i) vacuum magnetic fields for all regions, (ii) equilibrium magnetic fields inside of LCFSs, and (iii) equilibrium magnetic fields and 3-D potential variations. The circles indicate the ionization points of injected ions, whose spatial differences are less than 1cm as in the magnification.

of the LCFSs, as is usual for plasma simulations. On the other hand, the modification of the magnetic fields is small outside of the LCFSs, so it is convenient to use the vacuum fields to cover wider region in the vacuum vessel. In this sHIBP, we combine to use the equilibrium fields inside of the LCFSs and the vacuum fields outside of the LCFSs. This combination is easy to be implemented by using the module structure of iTDS. Figure 1 shows the comparison of the cases with the combined fields and only with the vacuum fields. The difference is rather small, considering the resolution of experimental detectors. The comparison between the cases with and without potential variation Φ_1 is also included in Fig. 1 to confirm little effect of the perturbed electric fields on the heavy ion trajectories. This is because the injected ion energy (several MeV) is much larger than the plasma potential (several 10 eV for the maximum). In this way, the effect of the 3-D variations is evaluated to find out the observation points of HIBP. Interactive evaluations of density and magnetic fluctuations are also possible, which are important to identify errors of experimental observations.

In sHIBP, variation of the beam energy (velocity of the heavy ions) and attenuation rate of the beam intensity are evaluated to give information of the plasma potential and density along the HIBP trajectory, as in Fig. 2. The magnetic fields (b), electrostatic potential (c) and electric fields (d) (spatial derivatives of the potential) are input parameters for the sHIBP, in which the set of the equations of motion is solved to calculate the trajectories. The connection of the vacuum and equilibrium fields at the LCFSs gives little discontinuity in the magnetic fields as in Fig. 2(b). The moment of the ionization from charge number +1 to +2 is indicated by the dashed line in Fig. 2. Figure 2(e) shows change of the heavy ion velocity along the trajectory, corresponding to the plasma potential profile in Fig. 2(b). The sudden change of the effective potential at the ionization point gives difference of the energies between the injected and detected heavy ions as in Fig. 2(e), which gives observation of the potential value at the ionization point. Noted that the non-smooth lines in Fig. 2(d) is due to usage of data on the meshes with finite intervals, which cause numerical errors for calculations. The Φ_0 variation is 10^{-3} orders of magnitude smaller than the injected beam energy, so is observable in experiments, but the Φ_1 variation from FORTEC-3D simulation is 10^{-6} orders of magnitude smaller than the injected beam energy, so is too small for detection. The detected beam intensity is given as

$$I_S = I_p A_p A_s \frac{\langle \sigma_{p\to s} \mathrm{v}_r \rangle}{\mathrm{v}_b} n(r_s) \Delta l , \qquad (2)$$

where I is the beam intensity, v_b is the beam velocity, v_r is the relative velocity, $\sigma_{\mathrm{p}\to\mathrm{s}}$ is the collisional cross-section of the ionization from the primary beam to the secondary beam, $n(r_s)$ is the density at the ionization point, Δl is the effective reaction path length of the ionization process, and the lower suffixes $i = p$ and s denote the primary and secondary beams, respectively. Beam attenuation rate A_i is given with

$$A_i = \exp\left(-\int_{L_i} \frac{\langle \sigma_i \mathrm{v}_r \rangle}{\mathrm{v}_b} n dl \right), \qquad (3)$$

where L_i is the path length along the trajectory. Figure 2(a) shows attenuation rates of the primary and secondary beams ($\ln A_i$). Multiplication of A_p, A_s and the reaction rate at the ionization point gives the detected beam intensity. For assessment of observability in the experiment, the intensity of the detected beam is evaluated in sHIBP. The detected beam intensity must be large enough for observation, and is predicted to be larger than the noise level given by the detector.

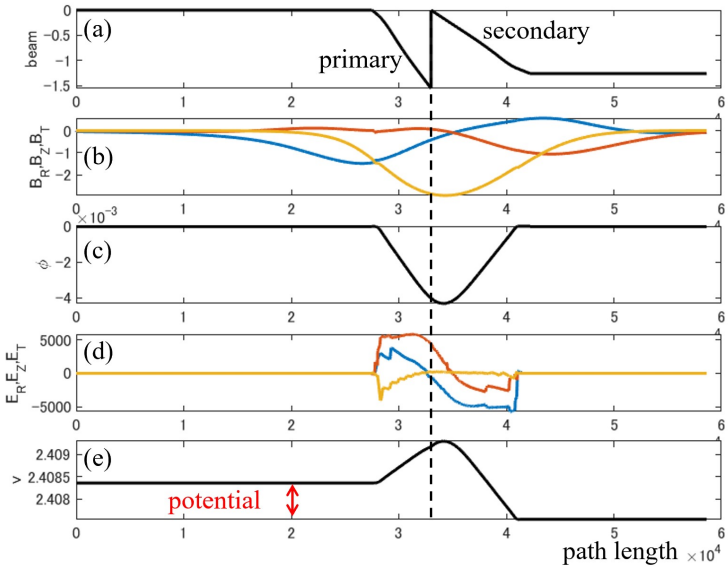

FIG. 2. Variations along the heavy ion trajectory. (a) Attenuation rate of the primary and secondary beams (ln A_i), (b) magnetic fields [T], (c) electrostatic potential [MeV], (d) electric fields [V/m], and (e) heavy ion velocity [10^6 m / s] are shown. The vertical dashed line indicates the position where the ionization occurs from charge number +1 to +2.

The observation points depend on the injection conditions of the heavy ions, so the profile scan can be made. The deviation of the potential values from the mean radial profile comes from Φ_1, which depends on the observation point. 2-D profile scan is also possible with change of the injected beam energy. Beam intensity includes effects of (1) damping in the primary and secondary paths, and (2) ionization rate at the ionization point, so comparison between the potential variation and beam intensity gives information on relative strength of effects (1) and (2).

Acknowledgements

This work was partially supported by JSPS KAKENHI JP17H06089, JP20K03905, and the collaboration program of NIFS (NIFS22KIST029, NIFS23KIST049) and of RIAM of Kyushu University. Some calculations were carried out using the JFRS-1 supercomputer system at IFERC-CSC in QST and Plasma Simulator supercomputer system in NIFS.

References

[1] LIN, L., *et al.*, Phys. Plasmas **16** (2009) 012502.
[2] HOLLAND, C., *et al.*, Phys. Plasmas **16** (2009) 052301.
[3] ROST, J. C., *et al.*, Phys. Plasmas **17** (2010) 062506.
[4] KRUTKIN, O.L., *et al.*, Nucl. Fusion **59** (2019) 096017
[5] KUDASHEV, I., *et al.*, Appl. Sci. **12** (2022) 9807.
[6] KASUYA, N., *et al.*, Plasma Sci. Tech. **13** (2011) 326.
[7] KASUYA, N., *et al.*, Nucl. Fusion **58** (2018) 106033.
[8] KASUYA, N., *et al.*, Proc. BPSI meeting (2022) PA-5.
[9] YOSHIHARA, N., *et al.*, Proc. BPSI meeting (2023) PA-5.
[10] IDO, T., *et al.*, Rev. Sci. Instrum. **77** (2006) 10F523.
[11] FUJITA, K., *et al.*, Nucl. Fusion **61** (2021) 086025.
[12] HIRSHMAN, S.P., *et al.*, Comput. Phys. Commun. **43** (1986) 143.

Extraction of abrupt turbulence driven particle transport using multi-field SVD

T. Kodahara[1], M. Sasaki[1], Y. Kawachi[2], Y. Jajima[1], T. Kobayashi[3], Y. Kosuga[4,5], G. Yatomi[6], M. Nakata[3,6,7], T. Yamada[5,8], H. Arakawa[9], A. Fujisawa[4,5]

[1]Nihon Univ., [2]KIT, [3]NIFS, [4]RIAM Kyushu Univ., [5]RCPT Kyushu Univ., [6]SOKENDAI, [7]RIKEN iTHEMS, [8]FAS Kyushu Univ., [9]FMS Kyushu Univ.

1. Introduction

Transport in magnetized plasma is often accompanied by abrupt behaviors such as ELM and breathers. Given the damage to the device wall caused by such transport, it is important to understand and predict the abrupt transport. However, since abrupt transport is spatiotemporally localized, Fourier analysis is generally unsuitable because it introduces many degrees of freedom. Therefore, decomposition in fractional degrees of freedom by data-driven scientific methods is easy to understand.

In this study, we propose the abrupt transport extraction method based on singular value decomposition (SVD) [1, 2], which is one of the data-driven scientific methods. Density fluctuations and radial flow fluctuations evaluated by the linearly magnetized plasma apparatus PANTA are used as targets. The radial flow fluctuation is evaluated from the electrostatic potential by using the E×B drift process. Both fluctuations are decomposed by the same basis function using SVD, and the abrupt transport is evaluated from product of each mode.

2. Multi-field SVD

The SVD is a diagonalization of a general matrix. Observables with spatio-temporal structure can generally be described as $\phi(\boldsymbol{x}, t)$; by using SVD for ϕ, it can be decomposed based on basis functions as follows [1, 2]

$$\phi = U\Sigma V^T \tag{1}$$

where Σ=diag(σ_1, σ_2, ..., σ_k), represented as a diagonal matrix (σ_1>σ_2>...>σ_k>0). The spatial structure U_k and time evolution V_k corresponding to each σ_k are also obtained. To extend the SVD to multiple fields, we combine multiple physical quantities as follows.

$$X = [f_1(\boldsymbol{x}, t_1), \cdots, f_1(\boldsymbol{x}, t_n), f_2(\boldsymbol{x}, t_1), \cdots, f_2(\boldsymbol{x}, t_n)] \tag{2}$$

Using SVD for matrix X, the decomposition is based on common basis function; a multiple-field

SVD was used for the density fluctuations N and radial flow fluctuations V_r obtained from PANTA [3, 4]. By multiplying each singular value $\sigma_k U_k V_k^T$, SVD modes N_α and $V_{r,\beta}$, which represent the spatio-temporal structure at mode k, are obtained [5, 6].

The mode-by-mode product of both physical quantities yields the transport matrices $\Gamma_{r,\alpha,\beta}$, which represent the contribution to transport driven by each mode combination. Where α, β are the mode indices of the density fluctuation N_α in mode α and the radial flow $V_{r,\beta}$ in mode β, respectively. By decomposing the transport matrix into a diagonal component $\Gamma_{r,diag}$, with equal and α and β other off-diagonal components $\Gamma_{r,off}$, we can decompose it into stationary and abrupt components of transport. The spatio-temporal structure of both transport components can also be discussed by summing over α and β as follows [7].

$$\Gamma_{r,diag} = \sum\nolimits_{\alpha} N_\alpha V_{r,\alpha} \tag{3}$$

$$\Gamma_{r,off} = \sum\nolimits_{\alpha \neq \beta} N_\alpha V_{r,\beta} \tag{4}$$

3. Off-diagonal component transport

We discuss the off-diagonal components of the transport matrix. For the spatio-temporal structure of the off-diagonal component transport, a two-dimensional Fourier mode decomposition reveals a broad spectrum in both the azimuthal and frequency directions. This means that short-lived structures appear in time and space. In addition, the spectrum extends in the positive wavenumber direction, indicating that it propagates in the positive direction. This corresponds to the electron-antimagnetic direction, which is consistent with the direction of oscillation propagation. In addition, the time evolution at a certain azimuthal point shows intermittent large amplitude transport. Compared to the time average of the diagonal component in the transport matrix, the transport is about 100 times more frequent.

Next, the behavior of the oscillations when abrupt transport occurs in the off-diagonal component is investigated. From the transport matrix, we extract the modes that contribute to the abrupt transport and compare the temporal and spatial behavior of the abrupt-driven mode and the off-diagonal component transport in both oscillations. Figure 1 (left panel) shows the time evolution of the off-diagonal component transport and both fluctuations. In the off-diagonal component, when abrupt transport occurs, the amplitude of both fluctuations is large and in phase with each other. The duration of the abrupt transport is about 1/10 of the fluctuation period and occurs instantaneously. The spatial structure of the abrupt transport when it occurs is also compared with that of the fluctuation. Figure 1 (right panel) shows the spatial structure of the off-diagonal component and both fluctuations. In the spatial structure, it can be seen that the amplitudes both fluctuations are large and in phase with each other when abrupt transport occurs. In addition, the peak width of the abrupt transport is about 1/5 of the wavelength of the

turbulence and is spatially localized. Thus, the decomposition into nonlinear modes using SVD allows us to identify such modes that drive the abrupt transport.

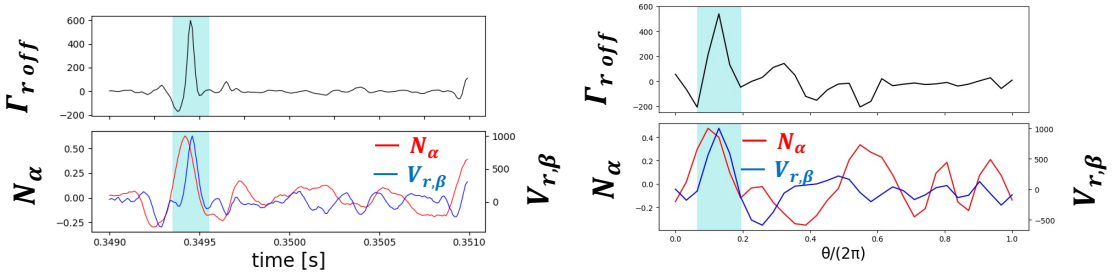

Figure 1 time evolution (left panel) and spatial structure (right panel) of off-diagonal component transport and both fluctuations. The red line represents the density and the blue line the radial flow. The amplitudes of both fluctuations are large in time and space, and abrupt transport occurs at the moment of phase coincidence.

Reference

[1] M. Sasaki, et al., Plasma Phys. Control. Fusion, 63.2, 025004 (2020).

[2] Y. Asahi, et al., Physics of Plasmas, 28.1, (2021)

[3] S. Inagaki, et al., Scientific reports, 6.1, 22189 (2016).

[4] T. Kobayashi, et al., Plasma Fusion Res., 12, 1401019 (2017).

[5] G. Yatomi, et al., Plasma Phys. Control. Fusion, 65.9, 095014 (2023).

[6] T. kodahara, et al., Plasma Fusion Res., 18, 1202036 (2023)

[7] F. Kin, et al., Physics of Plasmas, 26.4 (2019)

Optimizations of NB deposition calculations in the integrated code

*Kazutoshi Kani, Takaaki Fujita, Atsushi Okamoto, Sota Takemoto, Ren Kadomatsu
Nagoya Univ.

1 Introduction

The calculation speed of integrated codes needs to be more accelerated for the application to real time control and to surveying parameters. As for TOTAL code utilized in our group, calculation for NBCD (Neutral Beam Current Drive) takes long time. Approximately 60% of the calculation time is used for the NBCD calculation. Neutral particles injected with NB into the plasma become fast ions through interaction with electrons and ions in the plasma, orbiting the torus, resulting in a plasma current. The conceptual diagram is shown in Fig.1. In this study, we optimized NBCD calculation through two approaches for faster code executing. First, investigation of optimal number of test particles. Second, modify the code to generate multiple fast ions along a single trajectory of beam atoms.

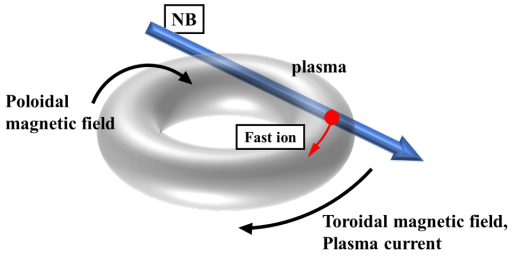

Fig.1 Conceptual diagram of NBCD

2 NBCD calculation methods

The conceptual diagram of determinating fast ion generation poiont is shown in Fig.2. The procedure of calculating NB current are the followings.

1. Finding fast ion generation point.
   i. Randomly generate a test particle on the cross-section of the ion source.(Cross-section of the ion source is divided into 200 sections in both r and θ derections.)
   ii. Calculating the non-ionization probability of a test particle along the beamline.
   iii. The point of fast-ion generation is set when the non-ionization probability falls below the ionization threshold (red line in Fig.3) determined by a random number in advance.
   iv. Repeating i∼iii for 10^4 times.
2. Determine the fast ion sourse.
3. Solving Fokker-Plank equation to obtain NB current drive density distribution.

Since the conditions for calculating the non-ionization probability, such as plasma temperature and density, depends on time and ion source cross-section location, the non-ionization probability must be recalculated each test particle.

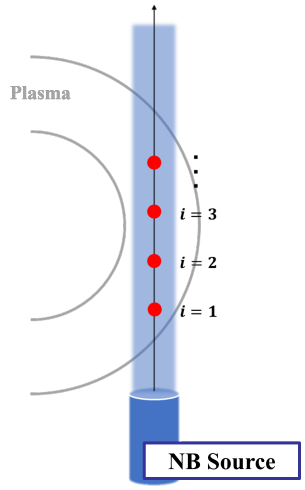

Fig.2 Conceptual diagram of fast ion generation point determination along the beamline.

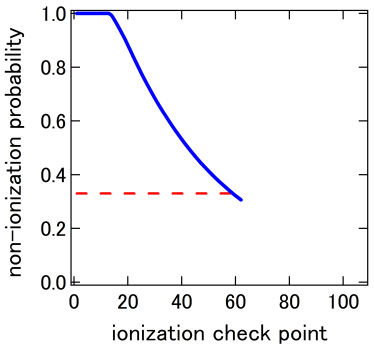

Fig.3 Conceptual diagram of finding the fast-ion generating point. The point where the blue line and the red line intersect is the point of fast-ion generation.

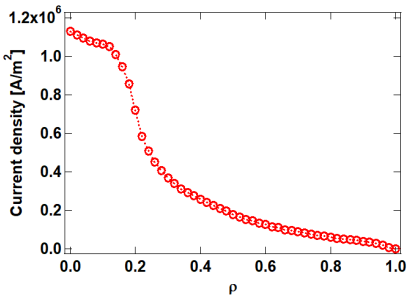

Fig.4 NB driven current density distribution at $t = 100$ s.

3 Optimization 1

The first optimization for speeding up the code is investigation of the optimal number of test particles. The way to investigate is as follows. First, run code with fewer test particles generated. Second, calculate the error rate in the NB-driven current density at each radial position. The error rate is defined as follow. $(\text{error-rate}[\%]) = \frac{\left|j_{NB_{10^4}} - j_{NB_n}\right|}{j_{NB_{10^4}}} \times 100$, where $j_{NB_{n(10^4)}}$ denotes NB current density in test particles $n(10^4)$. Then average computation time per step during the period with small change in plasma parameters. Finaly determine optimal number of test particles based on error rate and reduced computation time.

The results are shown in Fig.5. Fig.5 shows that there is approximate linear relationship between the number of particles generated and average computation time per step. We can reduce NB computation time by 65% by reducing the number of test particles to 1/10. And even if the number of test particles is reduced to 1/10, the error rate is about 4%.

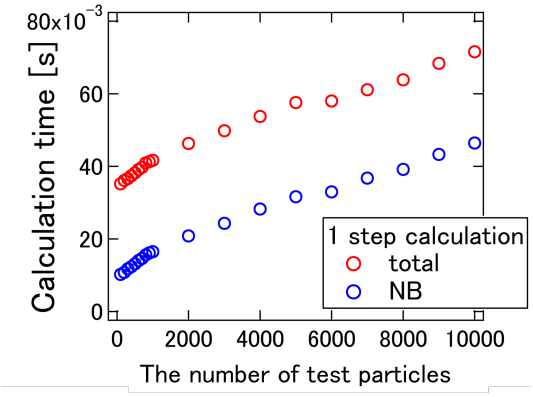

Fig.5 Relation between test particles and one step calculation time.

4 Optimization 2

The second optimization for speeding up the code is modify the code to generate multiple fast ions along a single trajectory of beam atoms. In a conventional method, firing one test particle from one point on the cross-section of the ion source to find one fast ion generation point at a step. We modified the code to set n test particles emitted from a single cross section point and to continue the calculation until all test particles have been ionized. (or, until the test particles penetrate the plasma.) The conceptual diagram of this new method is shown in Fig.6.

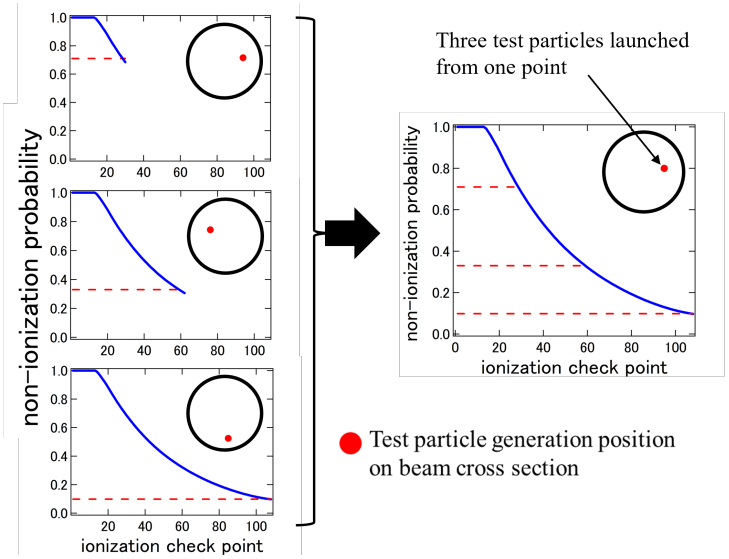

Fig.6 Conceptual diagram of optimization 2 ($n = 3$). Modified the code to allow n test particles to be fired from one point and n fast ion generation points to be obtained at a step.

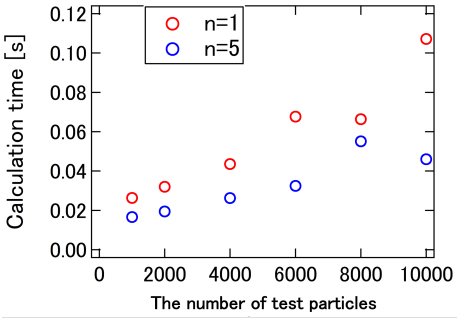

Fig.7 Relationship between the number of test particles per one test particle and the computation time per step for $n = 1$ and $n = 5$.

Figure 7 shows the relationship between the number of test particles per one test particle and the computation time per step for $n = 1$ and $n = 5$. We confirmed that applying this optimization could reduce calculation time. However, the appropriate value of n, or the possibility that this logic is inappropriate (since the computation time is longer in the new method with $n = 1$ than in the conventional method), is an issue for future reserch.

5 Summary and Prospect

In summary, we attempted to optimize the NB calculation using two approaches. First, we invested the optimal numbers of test particles. The results shows that reducing the number of test particles to 1/10 reduces NB computation time by 65%. Second, modifying the code to generate multiple fast ions along a single trajectory of beam atoms.

For the future prospects, we will determine the appropriate number of test particles emitted from a single cross section point. Also, parallelizing of non-sequential computation points is being considered.

Simulation of PCI experimental diagnostic for density fluctuations in tokamak plasmas

Kosuke KUWAMIYA[1], Naohiro KASUYA[1,2], Shota MOCHINAGA[1]
IGSES, Kyushu Univ.[1], RIAM, Kyushu Univ.[2]

1. Research background and objectives

Improving the confinement performance of plasma is crucial for the realization of nuclear fusion power generation. Since turbulent transport plays a significant role in the plasma confinement [1], understanding the turbulent transport is important. Phase Contrast Imaging (PCI) is one of the methods for measuring turbulence in magnetically-confined plasmas. For PCI, phase change of an injected laser beam is measured due to density fluctuations [2,3]. As PCI does not depend on specific plasma conditions and allows measurement across the entire plasma region, it has been adopted in various tokamaks and helical devices. Numerical simulations have also been conducted for comparison with experiments [2,4].

In this study, we perform PCI measurement simulations for experimental device JT-60SA. We simulate PCI measurements by combining magnetic field equilibrium calculations in the JT-60SA tokamak with fluctuation fields generated by a reduced MHD code as test data. Evaluation of the line integration effect in the direction of the line of sight for density fluctuations gives understanding of the signals obtained from PCI measurements.

2. Turbulence measurement simulation

We perform simulations of PCI measurements on fluctuation field data in a three-dimensional tokamak magnetic configuration. This section describes an overview of that process.

2.1 Plasma Equilibrium

For the simulation of measurements, the geometry of the device and the shape of the plasma are necessary. A tokamak plasma shape is calculated by using the integrated code TASK/EQU module. The EQU module is capable of performing equilibrium calculations for free-boundary plasmas, including the external coils currents [5].

2.2 Turbulence field

The turbulence to be measured is obtained by turbulence simulations. Here, we use pressure-driven ballooning type fluctuations calculated by using the reduced MHD code R5F [6]. Time evolution of five fields—potential, vector potential, parallel flow velocity, density, and electron temperature—are solved spatially in three dimensions using the vorticity equation, Ohm's law, the parallel ion motion equation, the continuity equation, and the electron temperature evolution equation. We use these fields as test data, although effects of the equilibrium shape are not included in the turbulence simulation.

2.3 PCI measurement simulation

The PCI measurement gives the wavenumber spectrum of density fluctuations [3]. The incident laser is scattered by the density fluctuations, and the interference of this scattered wave with the reference wave provides a two-dimensional pattern related to the wavenumber k of the fluctuation. Since the observation signal is integrated one along the line of sight, it becomes necessary to reconstruct local density fluctuation information from this signal. Here images of the density fluctuations integrated along the measurement line of sight are provided as the measurement results.

3. Results of data analysis

3.1 Equilibrium calculation

Figure 1 shows the magnetic field configuration obtained by using TASK/EQU. The coil currents used for the calculation are also shown in Table 1. In this case, the co-direction to the plasma current gives a positive value. The used parameters are major radius R = 3.0m, minor radius a = 1.2m, plasma volume V_p = 133m³, and toroidal magnetic field at the plasma center B_T = 2.25T, as for JT-60SA. As a result, an equilibrium magnetic field configuration with triangularity δ = 0.38 and elongation κ = 1.85 is obtained.

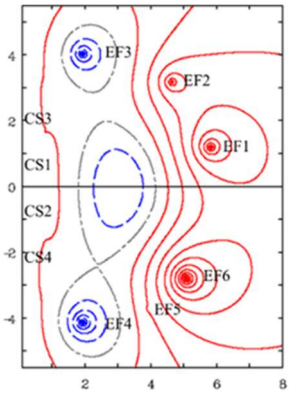

Fig. 1 Equilibrium magnetic field configuration

Table. 1 coil current

coil name	current(M A turn)
CS1	-1.08
CS2	-1.69
CS3	2.19
CS4	2.85
EF1	-3.62
EF2	-1.75
EF3	4.18
EF4	5.15
EF5	-0.135
EF6	-3.08

3.2 PCI measurement simulation

On the magnetic field equilibrium obtained by EQU, turbulence simulation data obtained by R5F is placed as the three-dimensional distribution of fluctuations (Fig. 2 (c)). In JT-60SA, the laser is injected tangentially to the magnetic field direction (Tangential Phase Contrast Imaging, TPCI) [2].

Using the TPCI beam path, as shown in Fig. 2, we calculate the integrated density fluctuation image. In JT-60SA, there is difference in the vertical direction of the injection and detection positions [2]. Therefore, in this simulation, we carry out the simulation along the path not horizontal. Figure 3 shows the snapshots of local (at the position B_3 in Fig.2) and integrated patterns of density fluctuations, and the calculated two-dimensional wavenumber spectrum from them. The axis x and y in Fig. 3 correspond to the direction perpendicular and horizontal to the line of sight, respectively.

Focusing on the two-dimensional wavenumber spectrum of the integrated one, peaks are observed at ($k_x\rho_i$, $k_y\rho_i$) = ($\pm$ 0.54, $\pm$ 0.18). Converting $k_x\rho_i = \pm$ 0.54 to wavelength gives $\lambda_x \approx$ 0.035 m, which matches the wavelength of the fluctuation in the x-direction of the local data. This indicates that fluctuations of this scale appear in the spectrum. On the other hand, converting $k_y\rho_i = \pm$ 0.18 to wavelength gives $\lambda_y \approx$ 0.10 m, which corresponds to the beam width (0.10 m). Actually, the wavelength of the dominant component in the y-direction is 0.20 m, so is not possible to be resolved in this measurement.

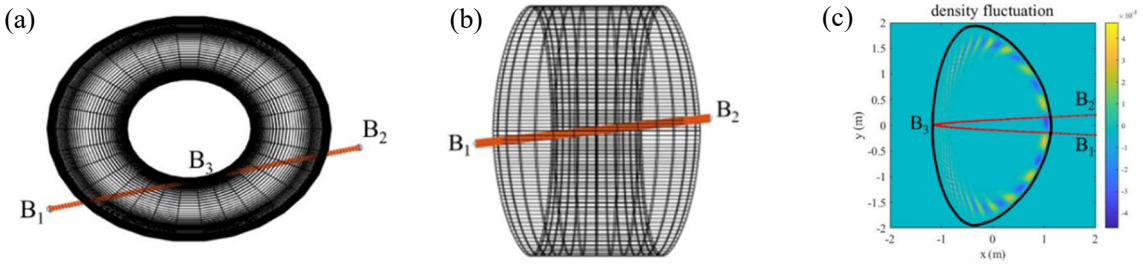

Fig. 2 TPCI measurement line of sight (orange lines). The views from (a) above and (b) the side are shown, with B_1 representing the laser incidence position and B_2 the detection position. The fluctuations and the line of sight on the poloidal cross-section are also shown in (c).

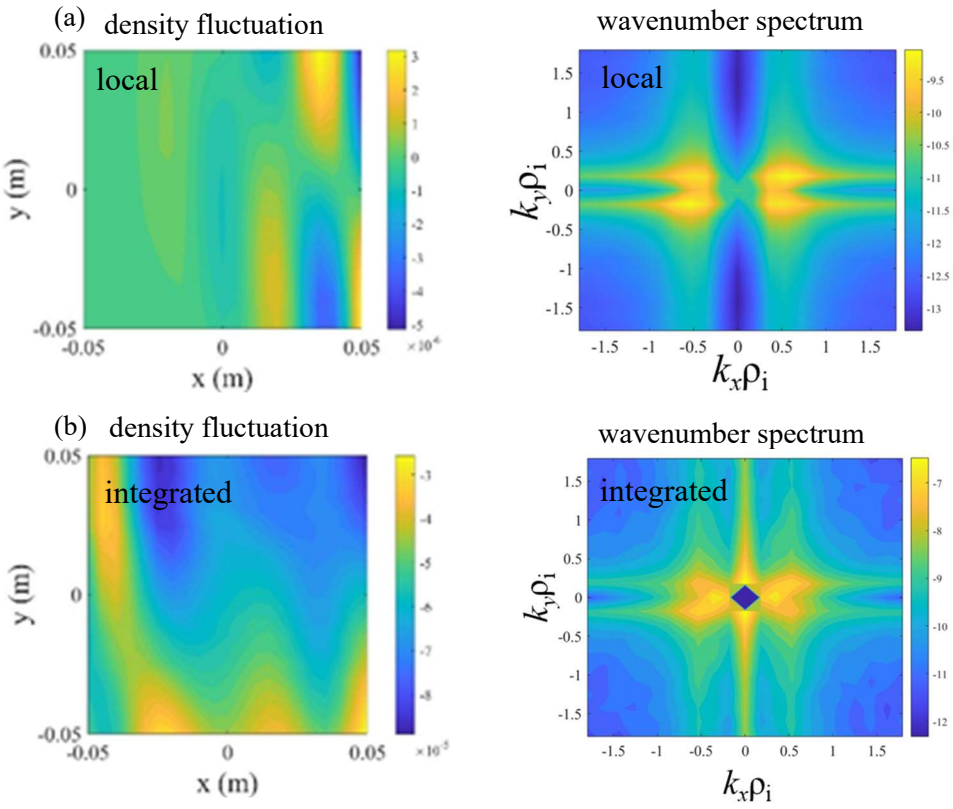

Fig. 3 Density fluctuations. Local and integral images and their wavenumber spectra are shown.

4. Conclusion

In this study, we constructed a PCI measurement simulation routine and performed calculations using the magnetic field configuration of JT-60SA tokamak plasma. We applied the TPCI diagnostic arrangement as in JT-60SA, and presented the local and line-of-sight integrated density fluctuations, as well as their two-dimensional wavenumber spectrum.

In the future, we will develop a routine to construct local information from the integrated density fluctuation data. We can utilize the fact that the direction of the magnetic field lines changes in relation to the measurement line of sight. Moreover, by analyzing microscopic turbulence simulation data considering the magnetic field configuration, we aim to deepen our understanding of turbulent transport caused by plasma instabilities.

References

[1] P. H. Diamond, *et al.*, Plasma Phys. Control. Fusion **47**, R35 (2005).

[2] S. Coda, *et al*, Nucl. Fusion **61**, 106022 (2021).

[3] K. Tanaka, *et al.,* Rev. Sci. Instrum. **79**, 10E702 (2008).

[4] N. Kasuya, *et al*., Nucl. Fusion **58**, 106033 (2018).

[5] 松岡啓介, 九大応力研所報 **141** 51 (2011).

[6] M. Yagi, *et al.*, 26th IAEA FEC, TH/P3-21 (2016).

Evaluation of nonlinear mechanism to induce inward turbulent particle fluxes in tokamaks

R. Miyamoto[1], N. Kasuya[1,2], M. Yagi[3]
[1]IGSES Kyushu Univ., [2]RIAM Kyushu Univ., [3]QST.

1. Introduction

In a fusion reactor, identifying an effective method for particle supply to core plasma is an important issue to maintain high density plasma. The pellet injection method is one of the ways to supply fuels to the core. With pellet injection, peaked density profiles are transiently formed and associated fluctuations have been observed [1]. In such regions, it is known that a particle flux toward the center is generated by fluctuations [2]. Therefore, a global turbulence simulation was conducted to evaluate the nonlinear mechanism of density fluctuations, which drive particle fluxes [3].

2. Simulation model

The reduced MHD code R5F [4] is used for the simulations. The code solves the time evolution of 3-D fields (electrostatic potential ϕ, vector potential in the magnetic field direction A, velocity in the magnetic field direction V, density N, and electron temperature T_e) using the following vorticity equation, ohm's law, equation of ion motion in the magnetic field direction, continuity equation, and evolution equation for electron temperature;

$$\frac{d}{dt}\nabla_\perp^2\phi = -\nabla_\parallel\nabla_\perp^2 A + \mu_{i\perp}\nabla_\perp^4\phi - [2rcos\theta, p] - \frac{q}{\varepsilon}\mu_i\frac{1}{r}\frac{\partial}{\partial r}r\left\{v + \frac{q}{\varepsilon}\frac{\partial\phi}{\partial r}\right\} - \frac{q}{\varepsilon}\frac{m_e}{m_i}\mu_e\frac{1}{r}\frac{\partial}{\partial r}r\left\{v + \delta\nabla_\perp^2 A + \frac{q}{\varepsilon}\frac{\partial(\phi - \delta p_e)}{\partial r}\right\}, \quad (1)$$

$$\frac{d}{dt}\left(A - \delta^2\frac{m_e}{m_i}\nabla_\perp^2 A\right) = -\nabla_\parallel(\phi - \delta p_e) + \eta_\parallel\nabla_\perp^2 A - 4\mu_{e\perp}\delta^2\frac{m_e}{m_i}\nabla_\perp^2\nabla_\perp^2 A + \alpha_T\delta\nabla_\parallel T_e + \delta\frac{m_e}{m_i}\mu_e\left\{v + \frac{q}{\varepsilon}\frac{\partial(\phi - \delta p_e)}{\partial r} + \delta\nabla_\perp^2 A\right\}, \quad (2)$$

$$\frac{dV}{dt} = -\nabla_\parallel p + 4\mu_{i\perp}\nabla_\perp^2 V - \mu_i\left(V + \frac{q}{\varepsilon}\frac{\partial\phi}{\partial r}\right) - \frac{m_e}{m_i}\mu_e\left\{V + \frac{q}{\varepsilon}\frac{\partial(\phi - \delta p_e)}{\partial r} + \delta\nabla_\perp^2 A\right\}, \quad (3)$$

$$\frac{dN}{dt} + \beta\frac{dp}{dt} = -\beta\nabla_\parallel(v + \delta\nabla_\perp^2 A) + \eta_\perp\beta\nabla_\perp^2 p + \beta[2rcos\theta, \phi - \delta p_e], \quad (4)$$

$$\frac{3}{2}\frac{dT_e}{dt} - \frac{\beta_e}{\beta}\frac{dN}{dt} = -\alpha_T\delta\beta_e\nabla_\parallel\nabla_\perp^2 A + \chi_{e\perp}\nabla_\perp^2 T_e + \epsilon^2\chi_{e\parallel}\nabla_\parallel^2 T_e - \frac{5}{2}\delta\beta_e[2rcos\theta, T_e], \quad (5)$$

where $d_t := \partial_t + [\phi, \ ]$, $\nabla_\parallel := \nabla_\parallel^{(0)} - [A, \ ]$. The set of equations is normalized by using the minor radius a for the length and by the poloidal Alfvén time $a/(\varepsilon v_a)$ for the time, where ε is the inverse aspect ratio and v_a is the Alfvén velocity. The calculation parameters used for the simulation are as follows; major radius R=1.5 m, minor radius r=0.5 m, beta value $\beta = \beta_e = 5 \times 10^{-3}$, inverse aspect ratio $\varepsilon = 0.33$, ion skin length $\delta = 10^{-2}$, mass ratio $m_e \,/\, m_i =$

$1/1836$, resistivities $\eta_\perp = 10^{-5}$, $\eta_\parallel = 10^{-5}$, thermal diffusion coefficients $\chi_{e\perp} = 10^{-5}, \chi_{e\parallel} = 10^{-5}$, neoclassical viscosity coefficients $\mu_{e\perp} = 10^{-5}, \mu_{i\perp} = 10^{-5}$, and thermal coefficient $\alpha_T = 0.71$. In this study, the calculations are carried out with an initial density profile peaked at radial position $r_s = 0.8$.

3. Analysis results

The initial density profile is set to be $N_{EQ} = N_0\,(1 - r^8\,)^8 + S_{amp}\exp(-\xi^2/2\Delta^2)$ with $\xi = r - r_s, r_s = 0.8, \Delta^2 = 0.003$, and the cases with $S_{amp} = 1.0$ and 1.5 are compared [3]. Figure 1 shows the radial profiles of the particle flux for $S_{amp} = 1.0$ and 1.5. In both cases, inward particle fluxes were observed around $r = 0.75$, where the safety factor is $q \cong 2.6$*. Figure 2 shows the time evolution of the particle flux at $r = 0.75$. The inward particle flux is about 10 times larger and is sustained for a longer duration for $S_{amp} = 1.5$ than $S_{amp} = 1.0$.

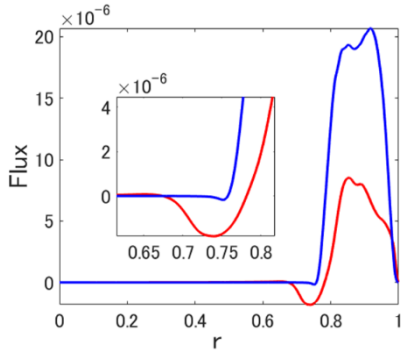

Fig.1 Radial profiles of the particle flux in the nonlinear states for $S_{amp} = 1.0$ and 1.5. Positive values correspond to the radially outward direction.

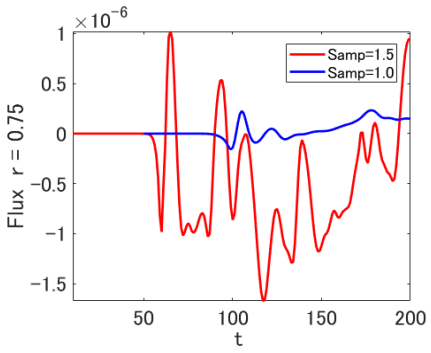

Fig.2 Time evolution of the particle flux for $S_{amp} = 1.5$ and 1.0 at $r = 0.75$

The turbulent particle flux Γ_{turb} is evaluated by the following equation from the nonlinear convective derivative term in the continuity equation.

$$\Gamma_{turb} = \sum_{m,n}\left\{(1+\beta)N_{m,n}\frac{\partial\phi_{-m,-n}}{r\partial\theta} + \beta A_{m,n}\frac{\partial v_{-m,-n}}{r\partial\theta} + \beta\delta A_{m,n}\frac{\partial\nabla_\perp^2 A_{-m,-n}}{r\partial\theta}\right\} \qquad (6)$$

Therefore, $(m,n) \neq (0,0)$ modes must be sustained for particle flux generation, where m is the poloidal mode number and n is the toroidal mode number. In this study, we focused on the density fluctuation of the first term in Eq. (6) because its contribution to the particle flux is relatively larger than other two terms. Figure 3 shows decomposition of the particle flux into contribution of each density fluctuation component. There are relatively low wavenumber modes, such as $(m,n) = (-3,1), (-5,2)$, and $(-8,3)$, which have larger contribution to the particle flux in the case $S_{amp} = 1.5$.

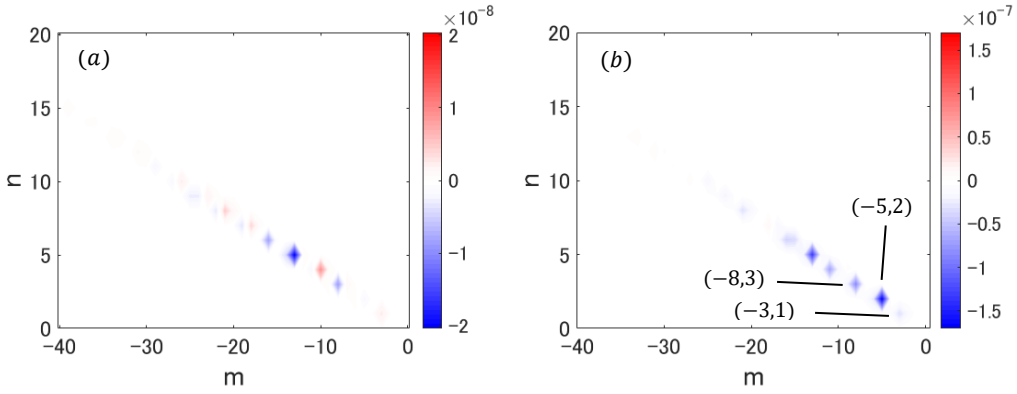

Fig.3 Decomposition of the particle flux into contribution of each density fluctuation components for cases $(a)S_{amp} = 1.0$ and $(b)\ S_{amp} = 1.5$

Figure 4 shows the nonlinear contributions to the $(-3,1)$ density fluctuation $(N_{-3,1})$ for $S_{amp} = 1.0$ and 1.5. Here, the averaged values for $t = 113\sim137$ and $t = 72\sim190$ are plotted for the $S_{amp} = 1.0$ and $S_{amp} = 1.5$ cases, respectively, corresponding to the time period when the inward fluxes are generated. Figure 4(a) shows that the nonlinear contribution of higher wavenumber components around $|m| \sim 20$ is significant in the $S_{amp} = 1.0$ case. On the other hand, Figure 4(b) shows that for $S_{amp} = 1.5$, there are various frequency components including lower wavenumber components that have significant influences, and their magnitudes are more than 10 times larger than those for $S_{amp} = 1.0$.

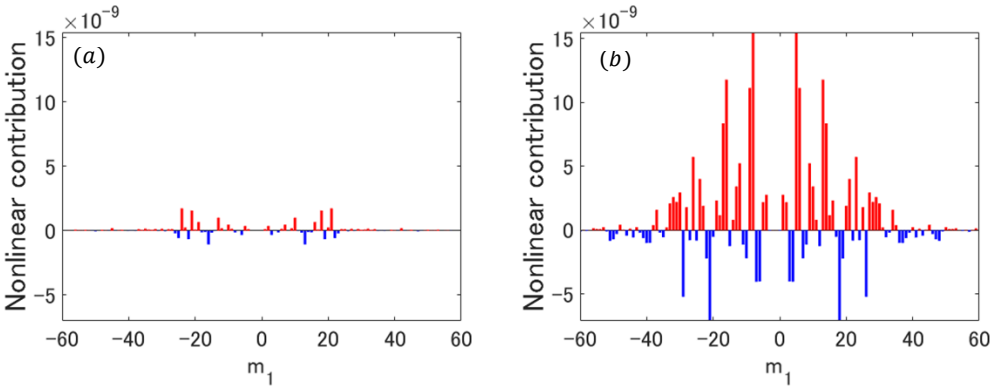

Fig.4 Nonlinear contributions to the (-3,1) density fluctuation for $(a)S_{amp} = 1.0$ and $(b)S_{amp} = 1.5$. The averaged values are plotted for the time period when inward particle fluxes are generated.

Next, the nonlinear contributions for the $S_{amp} = 1.5$ case are evaluated. Figure 5 shows that nonlinear contributions to $(a)\ (-3,1)$, $(b)\ (-5,2)$, $(c)\ (-8,3)$, and $(d)\ (-11,4)$ modes, which are rather lower wavenumber modes contributing to drive particle fluxes. Those are the average

component for $t = 72\sim190$. In this time period, the larger particle flux is sustained for $S_{amp} = 1.5$, compared with $S_{amp} = 1.0$. From Fig. 5, the following three-wave couplings are found to have significant contributions;

$$\begin{cases} (-3,1) \leftarrow (-8,3) + (5,-2) \\ (-5,2) \leftarrow (-11,4) + (6,-2) \\ (-8,3) \leftarrow (-11,4) + (3,-1) \\ (-11,4) \leftarrow (-14,5) + (3,-1) \end{cases}$$

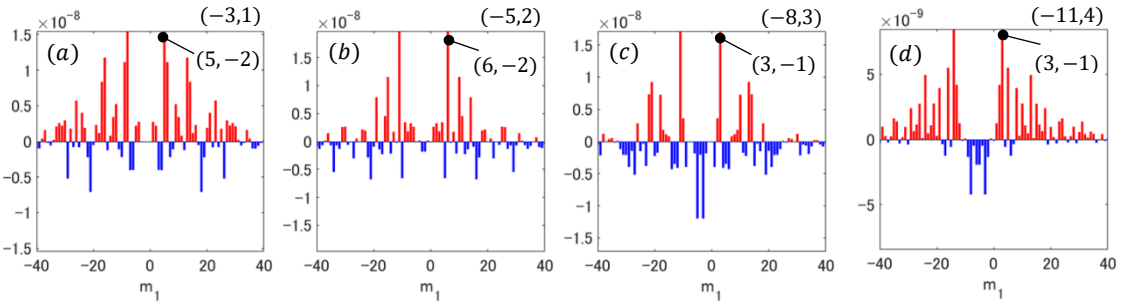

Fig.5 Nonlinear contributions to $(a)\,(-3,1)$, $(b)\,(-5,2)$, $(c)\,(-8,3)$, and $(d)\,(-11,4)$ modes for $S_{amp} = 1.5$.

Therefore, in the case of $S_{amp} = 1.5$, the fluctuation is sustained by the low wavenumber modes having a three-wave coupling relationship as in Fig.6, which induces a relatively larger inward particle flux for $S_{amp} = 1.5$ than for $S_{amp} = 1.0$.

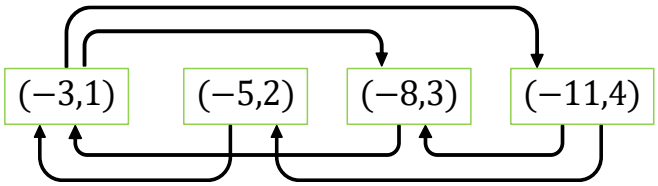

Fig.6 Three-wave coupling relationship for $S_{\mathrm{amp}} = 1.5$.

4. Conclusion

The R5F code was used to analyze the nonlinearly driven particle flux by electron drift mode. Nonlinear couplings are decomposed into contributions of each Fourier component. With the stronger density gradient case, when an stronger inward particle flux is driven, it is found that relatively lower wavenumber modes as $(m,n) = (-3,1),(-5,2),(-8,3)$ have large contributions and the fluctuations are sustained by their mode couplings.

Reference

[1] S. Ohshima, *et al*, Sci. Reps., **12** (2022) 14204.

[2] M. Yagi, *et al*, Proc. 16th BPSI Meeting (2018) 2-1.

[3] H. Todoroki, *et al*, Plasma Fusion Res. **18** (2023) 1203052.
[4] M. Yagi, *et al*, 26th IAEA FEC (2016) TH/P3-21.

Analysis of parallel flow shear driven mode including effect of finite ion temperature gradient

Itsuki OYAMA[1] and Yusuke KOSUGA[2]

[1]IGSES, Kyushu University

[2]RIAM, Kyushu University

1 Introduction

A good confinement requires transport barriers, for example external transport barrier (ETB) and internal transport barrier (ITB). As the experimental facts, it has been identified that there is such transport barriers in the experimental devices[1]. When transport barrier is built, plasma profiles get several kinds of gradients. Several mechanisms for losing transport barrier, especially ITB, are still missing. As the first step of understanding the cause to lose ITB, it is of importance to pay attention to a turbulent transport. This is because turbulent transport can affect the stability of ITB through some effect to the profile.

To shed light on it, we investigated how instability growth in the situation where three gradients (density, ion temperature and parallel velocity) coexist. It must be noted that parallel velocity gradient means the gradient of velocity parallel to the toroidal magnetic field lines.

2 Model

In this study, 3 gradients (density, ion temperature and parallel flow) are assumed. Especially we paid attention to the coexistence relation between ITG mode and PVG (Parallel Velocity Gradient driven) mode. To elucidate it, we use the set of fluid equations shown below :

$$\begin{cases} \dfrac{\partial}{\partial t}\dfrac{e\tilde{\phi}}{T_e} + v_E \cdot \dfrac{\nabla n_0}{n_0} + \nabla_\parallel \tilde{v}_\parallel - \dfrac{c}{B\omega_{ci}}\dfrac{d}{dt}\nabla_\perp^2\left(\tilde{\phi} + \dfrac{p_i}{en_0}\right) = 0 \\ \dfrac{d}{dt}\tilde{v}_\parallel + v_E \cdot \nabla V_\parallel = -\dfrac{\nabla_\parallel \tilde{p}_i}{m_i n_0} - \dfrac{e}{m_i}\nabla_\parallel \tilde{\phi} \\ \dfrac{3}{2}\left(\dfrac{\partial}{\partial t} + v_E \cdot \nabla\right)(P_0 + \tilde{p}) + \dfrac{5}{2}P_0\nabla_\parallel \tilde{v} + \dfrac{5}{2}P_0\nabla \cdot v_\perp^{(2)} + \nabla \cdot q^{(2)} = 0 \end{cases} \tag{1}$$

where $\tilde{\cdot}$ is a fluctuation. Subscripts, i or e, means ion and electron. e is the elementary electric charge. ϕ is the electrostatic potential. p is the pressure composed of density n and temperature

T. B is the magnetic field. ω_{ci} is the ion cyclotron frequency. First equation comes from the law of density conservation. Second one comes from the momentum equation in a parallel direction. Third equation comes from the law of energy conservation. Last two terms in third equation are already reported in *Pogtsue et al.*,[2]. It is to be noted that we assume the adiabatic response between electron density perturbation $\tilde{n}/n_0$ and electrostatic potential $e\tilde{\phi}/T_{e0}$.

3 Analysis

To elucidate which instability can be destabilized most, we derived the dispersion relation of this set of equations.

$$\begin{aligned}\left(1+\frac{10}{3}\rho_i^2k_\perp^2-\frac{5}{3}\frac{k_\parallel^2c_i^2}{\omega^2}\right)\left[1+\left(\tau+\frac{10}{3}\right)\rho_i^2k_\perp^2-\left(1+\frac{10}{3}\rho_i^2k_\perp^2\right)\tau\frac{\omega_{*i}}{\omega}+\rho_i^2k_\perp^2\tau\frac{\omega_{*pi}}{\omega}\right]\\ =\frac{k_\parallel^2c_i^2}{\omega^2}\tau\left(1+\frac{5}{3}\rho_i^2k_\perp^2\right)\left[1+\left(1+\frac{1}{\tau}\right)\frac{5}{3}\rho_i^2k_\perp^2+\frac{\omega_{*pi}}{\omega}-\left(1+\frac{10}{3}\rho_i^2k_\perp^2\right)\frac{k_y\rho_i}{k_\parallel c_i}\langle V_\parallel\rangle'\right]\end{aligned} \tag{2}$$

where τ is the temperature ratio T_e/T_i. $\omega_{*pi}=(1+\eta_i)\omega_{*i}$. η_i is the ratio between density gradient and ion temperature gradient $d\ln T_i/d\ln n$ and ω_{*i} is the ion drift frequency.

As the first step of analysis, we supposed the long wavelength. This assumption leads to the reduction of Eq. (2) by using $\rho_i k_\perp \longrightarrow 0$. Then, Eq. (2) can get formed as :

$$1-\frac{\omega_{*i}}{\omega}-\frac{k_\parallel^2c_i^2}{\omega^2}\left[\frac{5}{3}+\left(1-\frac{k_y\rho_i}{k_\parallel c_i}\langle V_\parallel\rangle'\right)+\left(\eta_i-\frac{2}{3}\right)\frac{\omega_{*i}}{\omega}\right]=0 \tag{3}$$

where τ is assumed as 1 for this time. The situation $\tau\sim 1$ corresponds to the situation where ion and electron are in almost same temperature. To get the growth rate of instabilities, we calculated Eq. (3) numerically :

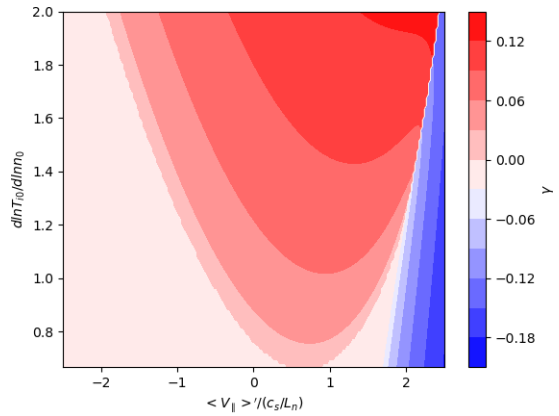

Figure 1: ITG mode dominated region.

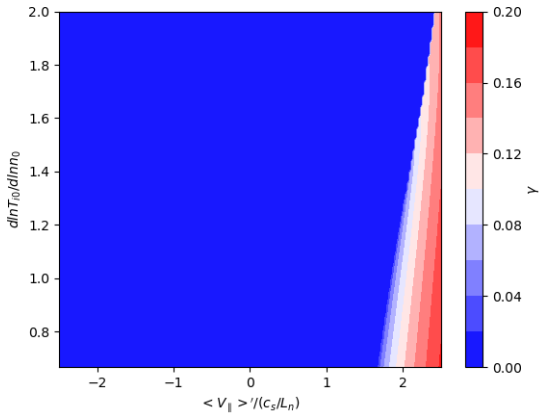

Figure 2: PVG mode dominated region

Because Eq. (3) is obviously cubic, there are three solutions for this. However one of three has negative growth rate ($\gamma \leq 0$), so it is omitted. In these graphs, the vertical axis corresponds to $\eta_i = d\ln T_i/d\ln n$ and horizontal axis corresponds to the strength of parallel velocity gradient $\langle V_\parallel \rangle'/(c_s/L_n)$. As it goes up in the vertical axis, ion temperature gradient is developed. As for the horizontal axis, parallel velocity gradient is developed most at both end.

In Fig. 1, as ion temperature gradient is surged, it is found that the value of growth rate goes higher. Then, we can recognize this as ITG mode. Paying attention to the lowest curve ($\gamma = 0$), the threshold of ITG mode goes higher, as velocity gradient is developed. This is why parallel flow shear stabilizes ITG mode. When parallel flow shear becomes strong enough to get ITG mode suppressed, we can see that situation in Fig. 2.

In Fig. 2, as parallel velocity gradient is developed, it is found that the value of growth rate goes higher. Then, we can recognize this as PVG mode. When η_i gets developed, the growth rate goes lower. This is why finite ion temperature gradient also stabilizes PVG mode.

Following the long wavelength assumption, we investigated the short wavelength scale. Although analysis of the long wavelength modes is important to understand general trend of instabilities, they are strongly affected by transport barriers. This is why analysis of the short wavelength is more important on condition that transport barrier exists. To calculate the growth rate, we utilized Eq. (2).

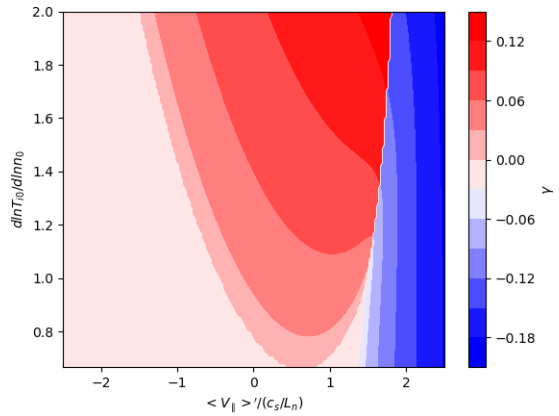

Figure 3: Short wavelength ITG mode dominated region.

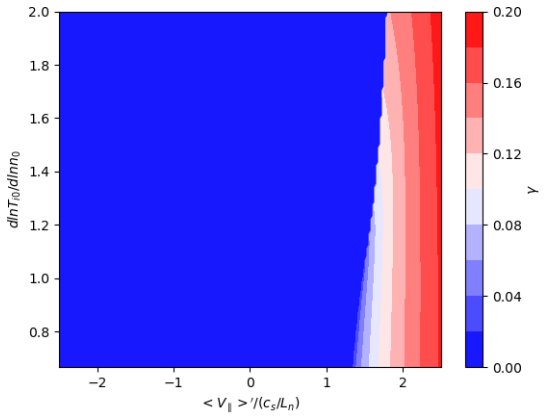

Figure 4: Short wavelength PVG mode dominated region

Here τ is still equal to 1. Compared Fig. 1 with Fig. 3, we can find the stabilization effects by parallel flow shear get strengthened. In addition, the ITG-damped region gets broader. In the same way as long wavelength, PVG mode gets destabilized in ITG-damped region. However this contour says the stabilization effects by η_i is reduced in comparison with the long wavelength case. Hence it can be said that the importance of PVG mode gets increased relatively.

Meanwhile it is also of note to consider the case where τ is finite. That situation is not so strange, because heating plasma techniques, e.g. Electron Cyclotron Resonance Heating (ECRH), can help τ to get finite. Furthermore, cold ion assumption has already been recognized, which ion temperature at edge plasma can be regarded as 0. In this case, τ is actually infinite. We can get the contour map with finite τ by using Eq. (2) below.

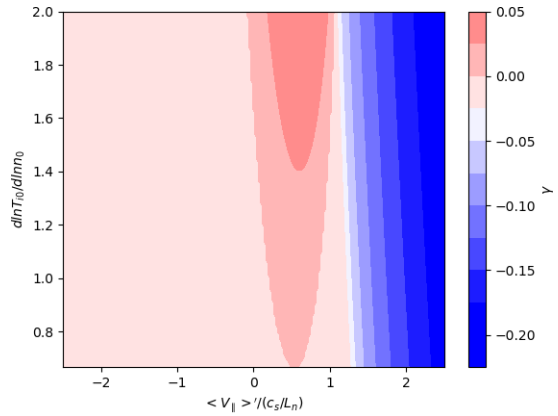

Figure 5: Short wavelength ITG mode dominated region. $\tau = 10$.

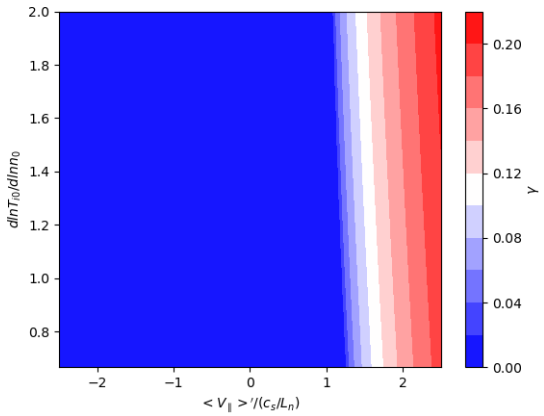

Figure 6: Short wavelength PVG mode dominated region. $\tau = 10$.

Compared Fig. 1 with Fig. 5, one easily sees that ITG mode gets nearly damped. Obviously the region, where ITG mode excites, gets shrunk, and the stabilization effect by parallel flow shear gets stronger in this region. Moreover the value of growth rate gets smaller even at most. Due to this, it is perhaps conceivable that ITG mode can not play a role as a source to drive transport in this case. In contrast, PVG mode get its region spread and significantly destabilized in that region. In that region, the stabilization effects by η_i is mostly gone. In consequence, it can be considered that PVG mode plays an important role as a driving source of transport in this kind of case.

This work is partly supported by the Grants-in-Aid for Scientific Research of JSPS of Japan (JP21H01066), the joint research project in RIAM, Kyushu University.

References

[1] K. Ida *et al.*, Plasma Phys. Control. Fusion (2018) **60** (3), 033001

[2] I. O. Pogtse *et al.*, J. Plasma Phys. **60** (1), 133-149 (1998)